



DRYP 2.0: A hydrological model for local and regional scale across aridity gradients

Edisson Andrés Quichimbo¹, Michael Bliss Singer^{1,3,4}, Katerina Michaelides^{2,4,5}, and Mark O. Cuthbert^{1,3,6}

Correspondence: E.A. Quichimbo (quichimbomiguitamaea@cardiff.ac.uk)

Abstract. The increasing demand for freshwater resources due to population growth, economic development, and climate change, requires more accurate representation and quantification of the key components of the water balance at relevant scales that goes beyond catchment domains. To address this need, we present DRYP 2.0 (DRYland water Partition model), a new version of a parsimonious, process-based, spatially distributed hydrological model (DRYP). DRYP 2.0 introduces several new capabilities, including the hydrological representation of small ephemeral ponds and large lakes, multiple interacting hydrogeological domains within a single-layer groundwater model, and vegetation canopy interception and evaporation to better capture the effects of vegetation on hydrology across different climatic gradients. Computational performance has also been enhanced through more efficient algorithms that reduce simulation time for long runs and/or over large spatial domains. We demonstrate these advances using high-resolution (1 km, 1 h) simulations over the Horn of Africa Dryland region (2,000,000 km²) as well as through various synthetic numerical tests. The results highlight the ability of the model, even without calibration, to reproduce global remote sensing data such as soil moisture, actual evapotranspiration, and total water storage, while also significantly reducing computation time. Furthermore, the explicit inclusion of multiple hydrogeological domains reveals important impacts on water table depth, with implications for improving global-scale simulations of the water balance.

1 Introduction

Accurate quantification of the water balance across local, catchment, and regional scales is essential for assessing water availability and understanding the impacts of climate variability on water resources (Niazi et al., 2024; Ferguson et al., 2020; Gleeson et al., 2020). Although large-scale hydrological models have significantly advanced our ability to simulate continental and global water cycles, they often overlook critical local processes that influence water availability and climatic hazards, which are believed to have a great impact on regional scales and across climatological gradients (Carroll et al., 2024; Cuthbert et al., 2019; Taylor et al., 2013). These local processes, including groundwater discharge in headwaters, transmission losses in channels, local and non-local groundwater recharge, and stream intermittency, are essential for capturing the spatial and tempo-

¹School of Earth and Environmental Sciences, Cardiff University, Cardiff, UK

²School of Geographical Sciences, University of Bristol, Bristol, BS8 1SS, UK

³Water Research Institute, Cardiff University, Cardiff, UK

⁴Earth Research Institute, University of California Santa Barbara, Santa Barbara, California, USA

⁵Cabot Institute for the Environment, University of Bristol, Bristol, UK

⁶Connected Waters Initiative Research Centre, University of New South Wales, Kensington, New South Wales, Australia



25

30



ral dynamics of regional hydrological systems. However, these processes remain underrepresented in most global and regional models due to limitations in model structure, spatial resolution, and computational resources (Quichimbo et al., 2020, 2021; Verkaik et al., 2024).

These process omissions are particularly problematic in dryland regions, where annual potential evapotranspiration rates greatly exceed annual precipitation rates, so soils dry out quickly between rainfall events and many streams run dry. In these environments, precipitation is generally delivered in short but intense events resulting in short-lived and highly variable runoff events (Shanafield et al., 2021; Arce et al., 2017). Processes such as groundwater recharge beneath ephemeral river networks, commonly called focused recharge, can therefore play an important role in the regional water balance and in determining water availability both at the surface and in the subsurface (Aryal et al., 2020; Arce et al., 2017; Shanafield et al., 2014). In addition, dryland hydrology is frequently influenced by non-local hydrological connectivity to humid headwater regions, where groundwater-surface water interactions in upland humid-climate rivers serve as the primary source of streamflow for downstream arid areas (Quichimbo et al., 2023; Xie et al., 2024). This non-local contribution is critical for maintaining baseflow and enabling groundwater recharge through transmission losses and overbank flooding in arid zones (Quichimbo et al., 2023). More broadly, widespread groundwater–surface water interactions play a central role in shaping the water balance in different ways across different climatic regions.

Groundwater–surface water interactions at local and regional scales are strongly governed by complex hydrogeological conditions. Aquifer systems are dependent on geological and tectonic features that frequently extend beyond surface catchment boundaries, thereby influencing intrabasin connectivity (Zarate et al., 2022; MacDonald et al., 2021; Bonsor et al., 2017; Condon et al., 2021). Neglecting this connectivity can significantly affect estimates of the water balance across scales. This is especially relevant in dryland environments, where deep water tables and lateral groundwater flow may contribute to river networks in lowland areas far from recharge zones (Cuthbert et al., 2019). Moreover, aquifer heterogeneity alters hydraulic properties with depth and thus influences lateral flow rates. For example, highly weathered crystalline basement systems often show declining transmissivity with depth as weathering diminishes (Abhervé et al., 2025). Taking into account this variability in hydraulic behaviour in different geological settings is essential to improve water balance quantification (Condon et al., 2021).

Groundwater–surface water interactions extend beyond river networks, making it equally important to quantify the role of large lakes in the regulation of water availability. This is particularly critical in endorheic systems, where lake storage is strongly influenced by exchanges with surrounding aquifers. Large lakes are commonly hydraulically connected to groundwater, and changes in their storage are controlled not only by climatological conditions but also by the dynamic hydraulic gradient between lake level and groundwater table elevation. Accurately representing these processes, including the emergence and desiccation of water bodies, is essential for improving water balance estimates.

Despite their importance, these mechanisms are often neglected in widely used global-scale models, such as those participating in the Inter-Sectoral Impact Model Intercomparison Project (ISIMIP2b) (Gosling et al., 2023a, b; Telteu et al., 2021). Current large-scale, process-based hydrological models face major challenges in representing low- and no-flow conditions (i.e., flow intermittency), largely due to the complexity of simulating bidirectional exchanges between groundwater and surface water, including lakes and reservoirs (Guo et al., 2024; Zaherpour et al., 2018). These interactions are controlled by dynamic





hydraulic gradients that are difficult to capture accurately, particularly at coarse spatial resolutions (Döll et al., 2016; Zaherpour et al., 2018). As a result, stream intermittency cannot be represented reliably without fine temporal and spatial resolution, limiting the ability of large-scale models to quantify water availability and its sensitivity to climate variability—information that is crucial for water management, decision-making, and ecosystem protection. Although basin-scale models can often address these limitations, the computational cost of solving the highly non-linear equations in physics-based approaches restricts their use over large domains such as continents.

Advancing regional-scale hydrological modelling therefore requires not only better process representation and higher spatial and temporal resolutions to capture key dynamics such as streamflow intermittency and groundwater—surface water exchanges, but also improvements in the numerical and computational efficiency of existing models (Bierkens et al., 2015; Döll et al., 2016; Verkaik et al., 2024). Achieving these improvements over large spatial extents remains difficult due to computational constraints and the limited availability of high-resolution climate and hydrological data. For instance, simulating daily streamflow in small headwater catchments may require grid cells as small as 500 m—a resolution feasible at basin scale but computationally prohibitive at continental or global scales (Mahoney et al., 2023).

To address these challenges, we present an updated version of the parsimonious, process-based, spatially distributed hydrological model DRYP (Dryland water Partition model). The model has previously demonstrated its utility in representing key dryland processes (MacLeod et al., 2023; Quichimbo et al., 2023, 2021), but here we extend its scope to simulate water partitioning across diverse regional and climatic settings. Key advances include the integration of processes relevant to both humid and arid regions, including vegetation canopy interception and storage, groundwater-lake interactions, groundwater typological characterisation, the emergence and dry-up of water bodies, and substantial gains in computational efficiency to support basin-and regional-scale applications at higher resolutions.

In the following sections, we first provide a brief overview of the model's capabilities and new features, with particular emphasis on the newly implemented components. We then present two examples of synthetic simulations—one for a spatially variable aquifer system and another for groundwater—lake interactions—to illustrate the use and capabilities of these two major updates. Additional examples are provided in the Appendix. This is followed by a real-world regional case study, and we conclude with a discussion of the model's broader applicability and potential future development pathways.

2 Methods

80

85

2.1 DRYP 2.0: Regional Water Partitioning Model

The main hydrological processes that control water fluxes and storage at local and regional scales across climatic conditions, and that are represented in DRYP 2.0, are illustrated in Figure 1a. DRYP 2.0 describes the movement of water through several storage compartments as follows: spatially distributed rainfall (P) from individual events is first intercepted by vegetation, an important process in humid regions that has been newly added to the model (Haas et al., 2024). Water stored in the canopy compartment (CZ) can be directly evaporated (E_{CZ}). Depending on precipitation intensity and duration, as well as the canopy storage capacity, throughfall (P_{th}) occurs. Once throughfall reaches the land surface (surface water compartment, SW), it is



100

105

110

120



partitioned into infiltration (I) and runoff (RO) according to precipitation characteristics and the water storage capacity in the unsaturated soil compartment (UZ) (Goodrich et al., 1997; Zoccatelli et al., 2019). Infiltrated water can be stored in the soil to support actual evapotranspiration (AET) or may percolate downward to recharge the groundwater (saturated compartment, SZ) as diffuse recharge (R_{dch}) once soil storage is exceeded.

Runoff is generated either as infiltration-excess flow, when rainfall intensity exceeds soil infiltration rate, or as saturation-excess flow, when infiltrated water exceeds soil storage capacity. Excess water is then routed to the nearest stream or water body along the topographic gradient. Along each stream reach, water can be added via baseflow (Q_{bf}) from groundwater or lost through the streambed as transmission losses (Q_{TL}) . The magnitude of both baseflow and transmission losses depends on the depth of the water table (Quichimbo et al., 2020). Beneath the streambed, a riparian compartment (RUZ) stores water at the interface between streams and the soil/groundwater. The riparian zone receives water from transmission losses, which increases soil moisture availability for evapotranspiration in river floodplains (AET_{rp}) . When riparian storage capacity is exceeded, excess water percolates to the groundwater, producing focused recharge (R_{fch}) (Schreiner-McGraw et al., 2019). When the water table is near the surface, capillary rise (ET_{SZ}) enhances water availability in both upland root zones and riparian areas.

DRYP 2.0 also incorporates a new water body compartment (PND), which is part of the surface water component. This compartment represents both shallow water bodies such as ponds and larger water bodies such as lakes that interact with the groundwater system. The interaction of large lakes with groundwater is driven by the hydraulic gradient between lake stage and water table elevation, whereas shallow emergent ponds are usually the result of surface runoff and are usually disconnected from the groundwater system.

Water movement in the SZ is governed by lateral flow, which is driven by the hydraulic gradient. Water movement in the SW is governed by the topographic gradient, and water movement in the UZ is governed by vertical gravitational flow. Anthropogenic interactions are also represented in DRYP as localized fluxes: abstractions from the saturated zone (Q_{ASZ}) , abstractions from streams (Q_{ASW}) and water bodies (Q_{PND}) , and irrigation added to the UZ (Q_{AUZ}) , with the latter applied to the surface and contributing to infiltration. These fluxes can be added at any location and time.

DRYP 2.0 can be forced not only with spatial fields of P and PET, but also with spatial fields of leaf area index (LAI) to drive the vegetation component. Water balance partitioning is determined by the interaction between these inputs and spatially distributed parameters representing topography, land cover, soil hydraulic properties, aquifer hydrogeology, and anthropogenic influences (Fig. 1b).

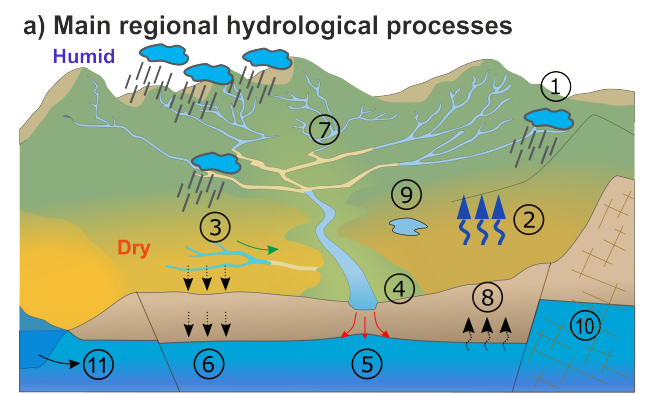
2.2 Model architecture

The model structure is organised into four primary components characterised by stores (Fig. 1c):

- i) the canopy store (CZ) representing the vegetation component, where precipitation is partitioned into throughfall and canopy evaporation;
 - ii) the surface water (SW) component, where throughfall/precipitation is partitioned into infiltration and overland flow, which is routed through the domain based on topography. The SW component included streams and water bodies (PND);







- Spatially variable rainstorms (1)
- High losses of precipitation by evapotranspiration in arid and semiarid areas (2)
- Brief and spatially variable runoff events in ephemeral drainage networks (3)
- Groundwater recharge through transmission losses (4) as focussed recharge (5).
- Spatially variable diffuse recharge (6)
- Groundwater discharge at head water streams (7)
- Groundwater evaporation from shallow water tables (8)
- Developmement of ponding conditions (9)
- Multiple aguifer systems (10)
- Groundwater lake water interactions (11)

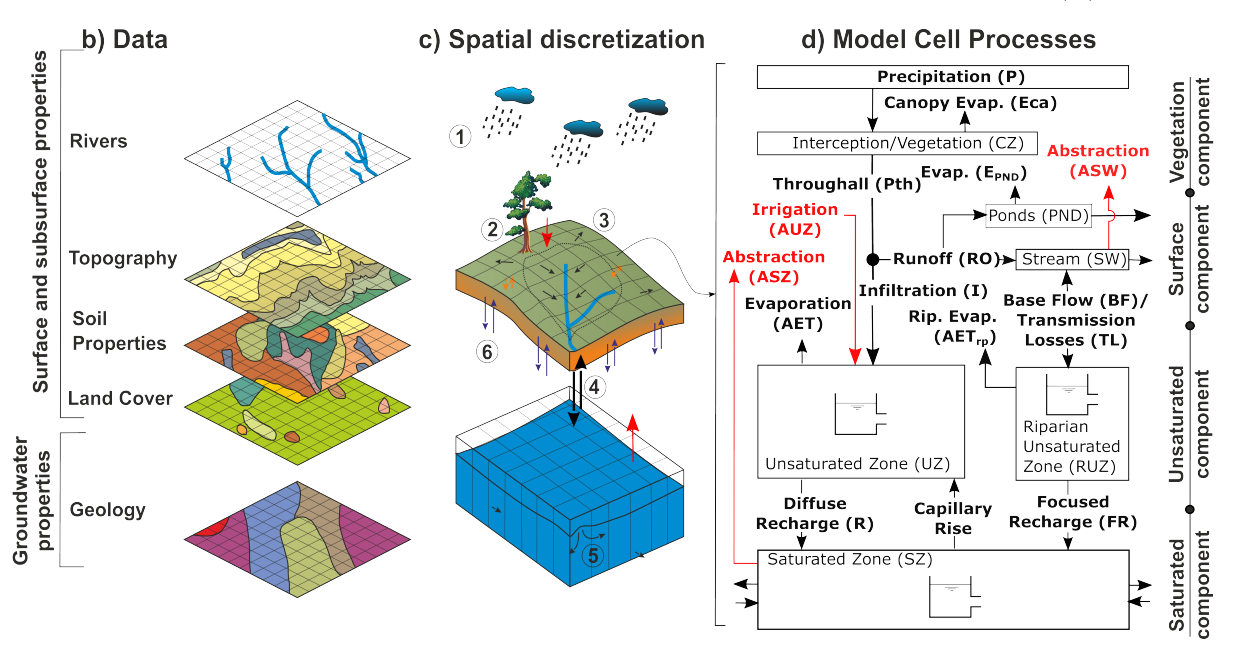


Figure 1. Schematic of DRYP 2.0 showing: (a) main hydrological processes controlling water partitioning at local and regional scales; (b) distributed datasets used to derive input parameters; (c) vertical and horizontal discretization illustrating topographically driven surface runoff, vertical flow in the unsaturated zone, and hydraulic gradient—driven groundwater flow in the saturated component; and (d) model structure and processes within a single grid cell, including interception, and surface, unsaturated, and saturated zone processes. Arrows indicate flow directions, and red lines represent anthropogenic fluxes. Modified from Quichimbo et al. (2021).

- iii) the unsaturated zone component that represents the soil (UZ) and riparian areas adjacent to streams (RUZ); and
- iv) the saturated zone (SZ) component representing groundwater flow.
- All four components are discretised using square grid cells and fluxes and stores are vertically integrated through the layers using a one-way sequential computational scheme (Fig. 1c). Despite the sequential structure, all components are hydraulically interconnected, allowing for gradient-driven and bi-directional water exchange (e.g., between SW and UZ) (Figs. 1c and 1d).





DRYP v2.0 also retains the original architecture of DRYP 1.0, developed in Python using the Landlab package (Barnhart et al., 2020; Hobley et al., 2017), which provides a gridded environment for representing the spatial variability of hydrological processes. The gridded domain consists of cells, which serve as the fundamental hydrological unit in DRYP. However, in DRYP 2.0 key components have been rewritten in the faster programming language FORTRAN to enhance computational performance.

The main advantage of the gridded layer-based structure is that it allows users to define the level of process complexity and the parameterization appropriate for a given application, as well as select suitable spatial resolution and time-stepping configurations. All grid cells can potentially include all process components shown in Figure 1d. However, stream and riparian components can be omitted if channel characteristics are not provided, in such cases, runoff generated in a cell is routed directly to the next downstream cell without additional interactions or losses. The size of the stream and riparian zones is only constrained by the grid resolution. If a stream channel is present within the cell, a riparian store (RUZ) is also included. The riparian zone is defined as a lateral area adjacent to the stream, with a user-defined width.

DRYP 2.0 also retains the four selectable infiltration methods to quantify precipitation partitioning: (i) Philip's equation, (ii) Green-Ampt equation, (iii) Upscaled Green-Ampt equation, and (iv) Shaake approach. This provides the user with the ability to further investigate and assess the influence of these different approaches. A full description of these approaches is provided in Quichimbo et al. (2021).

2.2.1 Interception

DRYP 2.0 includes a parsimonious interception approach based on Kozak et al. (2007) and is modelled by resolving the water balance at the canopy store (CZ) as follows:

$$\Delta S_{\rm CZ} = P - P_{\rm th} - E_{\rm ca} \tag{1}$$

where: ΔS_{CZ} is the change over time in canopy storage [L], P is precipitation [L T⁻¹], E_{ca} is canopy evaporation [L T⁻¹], and P_{th} is throughfall [L T⁻¹]. Here, throughfall is considered as all precipitation reaching the soil, therefore, it includes water dripping from leaves and branches, and stemflow.

Canopy evaporation is estimated based on the current canopy storage S_{CZ} [L], its maximum storage capacity S_{CZmax} [L], the reference evapotranspiration ET_0 [L T⁻¹], and vegetation fraction a_v [-]:

$$E_{\rm ca} = a_v \frac{S_{\rm CZ}}{S_{\rm CZ,max}} ET_0 \tag{2}$$

 S_{CZmax} can be derived using different methods based on direct measurements of precipitation, throughfall, and stemflow, or from remote sensing datasets (Vegas Galdos et al., 2012). DRYP 2.0 includes two selectable approaches for estimating S_{CZmax} based on the leaf area index (LAI, [L^2 L^{-2}]): the von Hoyningen-Huene (1981) approach:

$$S_{\text{CZmax}} = 0.935 + 0.498LAI - LAI^2 \tag{3}$$

or the Menzel (1996) approach:

$$S_{\text{CZmax}} = f^* \log \left(1 + LAI \right) \tag{4}$$





where f^* is a factor depending on the vegetation type.

160 2.2.2 Infiltration

170

The infiltration component has been updated by replacing precipitation with throughfall, thus it now partitions throughfall (P_{th}) into infiltration (I) and surface runoff (RO), according to the following mass balance:

$$P_{\rm th} = I - RO \tag{5}$$

Infiltration (I) is modelled as a function of soil properties, throughfall, and initial soil moisture conditions (θ_0) [L³ L⁻³] (Quichimbo et al., 2021).

2.2.3 Flow Routing and Transmission Losses

To support simulations over large spatial domains (e.g., regional to global scales), DRYP 2.0 incorporates an optimised flow routing component. This new module, implemented in FORTRAN, significantly improves computational efficiency by overcoming the performance limitations of Python when executing iterative processes such as those involving nested loops (Dalcin et al., 2011).

The flow routing component uses a 8-D flow direction approach allowing the water to move only to the next downstream cell (regardless of cardinal direction). Fluxes at each cell of the surface components are modelled using the following water balance equation:

$$\Delta S_{\rm OZ} = Q_{\rm RO} + Q_{\rm BF} - Q - Q_{\rm TL} - Q_{\rm AOZ} \tag{6}$$

where: ΔS_{OZ} is the change in surface storage [L³], Q_{RO} is surface runoff input from upstream cells [L³ T⁻¹], Q_{BF} is baseflow [L³ T⁻¹], Q_{IS} is discharge to the next cell [L³ T⁻¹], Q_{TL} is transmission losses [L³ T⁻¹], and Q_{AOZ} is surface water abstraction [L³ T⁻¹]. Note that Q_{RO} is calculated as the cumulative values of RO times the cell area of all upstream cells of the corresponding contributing area.

All cells include the streamflow component by default. However, the user can specify which cells contain streams by providing a river network map. For non-stream (hillslope) cells, the channel-related loss terms $Q_{\rm TL}$ and $Q_{\rm AOZ}$, as well as the storage term $\Delta S_{\rm OZ}$ in Eq. (6), are set to zero. Consequently, any overland flow generated in hillslope cells is routed instantaneously to the next downslope cell following the topographic gradient (i.e. assuming no storage or time delay in the overland flow process). For a detailed description of how $Q_{\rm TL}$ is estimated, the reader is referred to Quichimbo et al. (2021).

2.2.4 Unsaturated and Riparian Unsaturated Zones

The unsaturated zone (UZ) component is fully described on Quichimbo et al. (2021), however, a short description is presented here. The UZ component represents soil on both the hillslope areas and the riparian zones located immediately beneath stream channels. River cells are characterised by the riparian unsaturated zone, while non-river cells are characterised by the hillslope unsaturated zone. These two components are modelled separately using a linear reservoir approach, with the water balance





equation being conditionally adapted for each. The water balance equation governing the change in storage in the unsaturated zone is given by:

$$\Delta S_{\rm UZ} = I - AET - AET_{\rm rp} - R_{\rm fch} - R_{\rm dch} + \frac{(Q_{\rm TL} - Q_{\rm BF} + Q_{\rm AUZ})}{A_{cell}} \tag{7}$$

where: $\Delta S_{\rm UZ}$ is the change in storage of the unsaturated zone [L T⁻¹], I is infiltration [L T⁻¹], AET is actual evapotranspiration from hillslopes [L T⁻¹], $AET_{\rm rp}$ is actual evapotranspiration for riparian zones [L T⁻¹], $R_{\rm fch}$ is recharge for riparian zones to the saturated zone [L T⁻¹], $R_{\rm dch}$ is recharge for hillslope areas [L T⁻¹], $Q_{\rm BF}$ is groundwater discharge (baseflow) to streams [L³ T⁻¹], $Q_{\rm AUZ}$ is anthropogenic irrigation [L³ T⁻¹], and $R_{\rm cell}$ is the cell area [L²].

Equation 7 adapts depending on the component being modelled. For hillslope cells, the terms $Q_{\rm TL}$, $AET_{\rm rp}$, and $R_{\rm fch}$ are set to zero, as interactions with streams occur only in riparian cells. Conversely, for riparian zones, the terms $Q_{\rm AUZ}$, $R_{\rm dch}$, and AET are set to zero, as these fluxes are exclusive for hillslope areas.

Actual evapotranspiration (AET) is calculated based on vegetation stress using the FAO methodology (?):

$$200 \quad AET = \beta \cdot ET_0 \tag{8}$$

where: ET_0 is the reference potential evapotranspiration [L³ L⁻³], β is the vegetation stress coefficient defined as:

$$\beta = \begin{cases} \frac{\theta - \theta_{wp}}{0.5(\theta_{fc} - \theta_{wp})} & \text{if } \frac{\theta - \theta_{wp}}{0.5(\theta_{fc} - \theta_{wp})} < 1\\ 1 & \text{if } \frac{\theta - \theta_{wp}}{0.5(\theta_{fc} - \theta_{wp})} \ge 1 \end{cases}$$

$$(9)$$

with: θ is actual soil moisture [L³ L⁻³] at wilting point, θ_{wp} [L³ L⁻³], and field capacity θ_{fc} [L³ L⁻³].

 ET_0 can be estimated by multiplying the crop coefficient factor (K_c) by the potential evapotranspiration following Allen 205 et al. (1998).

2.2.5 Ponds, Small Lakes, and Surface Reservoirs

For modelling purposes, ponds are defined as shallow surface water bodies with surface areas less than or equal to the model grid cell size. Ponds receive water inputs from surface runoff and direct precipitation only. Water losses from ponds occur only through direct evaporation and/or anthropogenic abstractions. No lateral groundwater from adjacent cells is included.

To represent ponds within the model, an additional storage compartment is included in each grid cell. When the volume of water reaching a pond exceeds its maximum storage capacity, the excess is routed to the downstream cell. The water balance for ponds is given by:

$$\Delta S_{\text{PND}} = Q_{RO} + A_{\text{PNDmax}} P - E_{\text{PND}} A_{\text{PND}} - Q_{\text{PND}} - Q_{\text{APND}}$$

$$\tag{10}$$

where: ΔS_{PND} is the change in pond storage [L³], Q_{RO} is surface runoff from upstream cells [L³ T⁻¹], P is direct precipitation over the pond [L T⁻¹], Q_{PND} is excess water which is routed to downstream cells [L³ T⁻¹], E_{PND} is evaporation from the pond surface [L T⁻¹], Q_{APND} is water abstraction for anthropogenic use [L³ T⁻¹], Q_{PND} is the surface area of the pond [L²], and Q_{PND} is the maximum extend of the pond [L²]



225



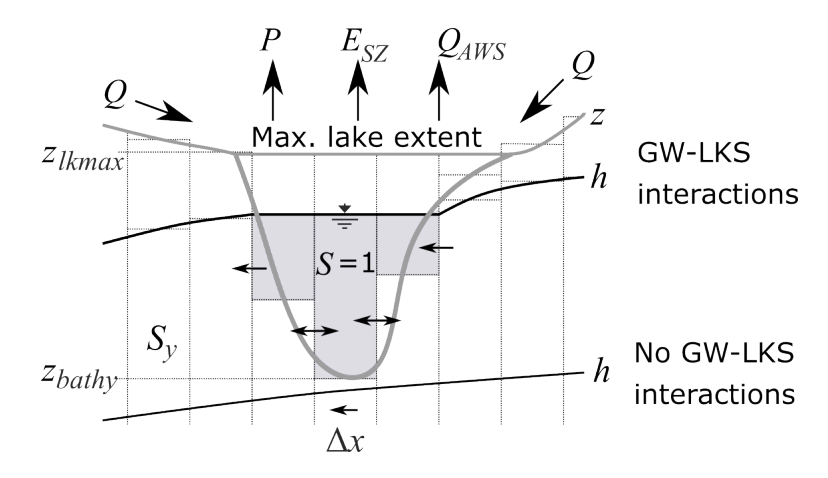


Figure 2. Schematic representation of groundwater-lakes water interactions including hydrological and lateral inflow/outflow fluxes. The shaded area represents the lake domain.

Pond storage capacity is parameterised based on two primary physical attributes: *maximum surface extent* and *maximum depth*. These parameters are used to calculate the maximum volume of water a pond can retain. DRYP 2.0 uses a potential function to characterise the relationship between area, depth and volume. A detailed explanation of the approach is presented in the appendix A3. Maximum extent and depth can be obtained from local and regional datasets (e.g., GLOBathy (Khazaei et al., 2022)) or manual delineation.

2.2.6 Groundwater-Lake interactions

In DRYP 2.0, 'lakes' are surface water bodies that interact with the groundwater system by imposing a variable-head boundary condition. As such, they can function either as sources of recharge or as discharge (sink) points for groundwater, depending on the hydraulic gradient. In the model, lakes are represented by designated cells that remain in contact with the groundwater during both emergence and drying-up phases, with an associated storage capacity assigned. These cells must be defined a priori by specifying the lake depth (bathymetry) (Figure 2).

Groundwater–lake (surface water) interactions (GW–LKS) are incorporated by coupling both groundwater–unsaturated zone (GW–UZ) and groundwater–surface water (GW–SW) interactions. Thus, to represent lakes within the model, an additional layer is added above the unsaturated (soil) layer. The key difference between the lake layer and the soil layer is that the lake layer has a fixed storage capacity of S=1.0. Its thickness varies dynamically based on the lake stage. To prevent spatial variation in stage level, it is assumed that any inflow to the lake is instantaneously distributed across the entire lake area.

$$\frac{\partial h}{\partial t} = P + Q - E_{SZ} - Q_{ASZ} - \nabla \cdot \left(-K_{aq} h(\nabla h) \right) \tag{11}$$

where: ∇ represents the differential operator, Q_{ASZ} is lake water abstraction [L³ T⁻¹]. A detailed description of the GW–LKS implementation is provided in Appendix A2.



245

250



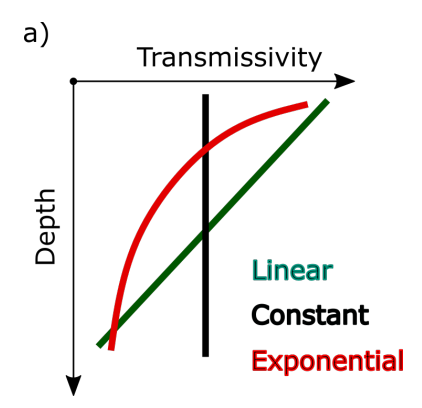


Figure 3. Transmissivity functions included in DRYPv2: Constant (C), linear (L), and exponential (E) function.

2.2.7 Spatially variable aquifer system types

Hydrogeological properties may exhibit substantial spatial and vertical variability across large regions. As a result, large-scale model domains often encompass a variety of aquifer systems such as unconsolidated sediments, consolidated formations, and fractured rock aquifers, which may be hydraulically interconnected (Condon et al., 2021; Macdonald et al., 2010; MacDonald et al., 2012). These aquifers typically show distinct hydraulic behaviours that influence groundwater flow and storage dynamics.

To improve the representation of these heterogeneous systems and their influence on subsurface water flow across a regional domain, DRYP 2.0 incorporates a set of transmissivity functions that characterise the depth-dependent behaviour of different aquifer types. Thus, three transmissivity formulations are included: (i) Constant Transmissivity, assumes transmissivity remains uniform with water table depth. This formulation is appropriate for aquifers where hydraulic conductivity and saturated thickness are relatively invariant (e.g., thick consolidated rock formations). (ii) Exponential Transmissivity Decay captures systems where transmissivity decreases significantly with depth, typical of fractured or weathered rock aquifers where permeability diminishes in deeper layers; and (iii) Linear Transmissivity change, represents constant depth-dependent changes in transmissivity, as seen in shallow unconsolidated sedimentary aquifers.

These transmissivity profiles can be assigned spatially across the model domain, enabling the simultaneous representation of multiple aquifer systems within a unified modelling framework. This approach enhances the model's ability to simulate groundwater dynamics in heterogeneous hydrogeological settings while retaining the one-layer structure used in DRYP 2.0.

2.3 Numerical simulations

A series of numerical examples has been developed to demonstrate the new model capabilities and their applications. Two synthetic examples are presented below: one illustrating the groundwater–lake interaction component (Sec. 2.3.1), and another illustrating a multi-aquifer system (Sec. 2.3.2). Additional examples for the canopy-interception and shallow pond components are provided in Appendix A4 and Appendix A5, respectively.





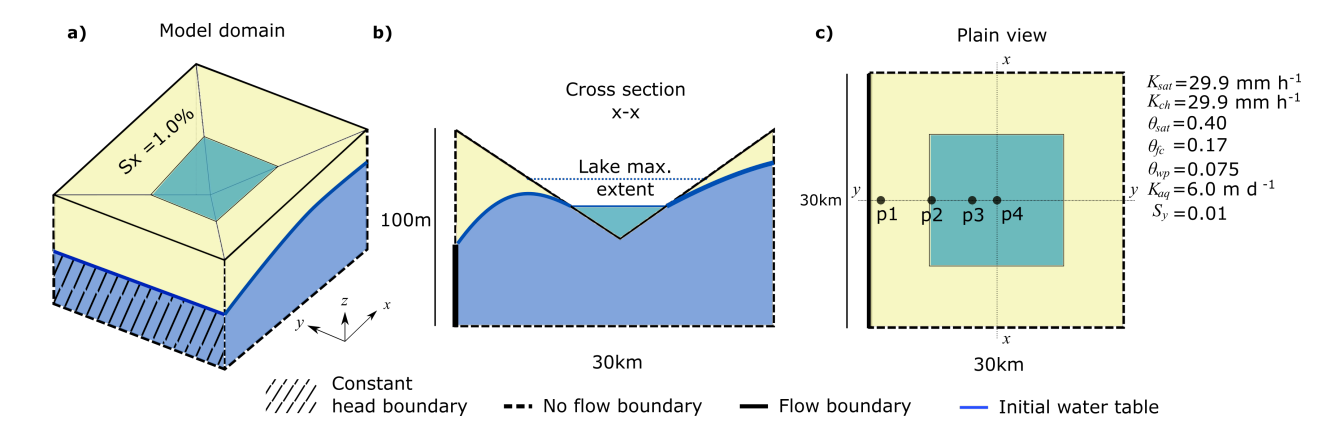


Figure 4. Model domain of the synthetic analysis of groundwater-lakes interactions (GW-LKS). (a) 3D view of the model domain, (b) cross section along the x-axis, and (c) plan view of the model domain indicating the location of monitoring points, p1-4, and x- and y-axis.

2.3.1 Groundwater - lake interactions

To illustrate the representation of the groundwater-lakes (surface water) interaction component, a synthetic experiment was performed. Synthetic experiments are useful to understand the behaviour of the model under hypothetical conditions (Clark et al., 2015). Thus, the main goal was to represent the impact of the lake as a boundary condition on the groundwater system.

The idealised model domain used for the simulation consisted of a land surface with a central depression representing the lake (Fig. 4). The domain was defined as a 30×30 grid with a cell size of 1 km. The lake was shaped as a tetrahedron, with its edges conforming to the extent of the model domain (Fig. 4). The boundary conditions of the model domain were specified as a constant head boundary on the left side and no-flow boundaries on the remaining sides. The bottom boundary was also specified as a no-flow condition (Fig. 4).

Synthetic time series of precipitation and potential evapotranspiration were used to force the model. The synthetic precipitation was defined as a rectangular step function with a rate of 0.60 mm h^{-1} and a duration of 10 days. Potential evapotranspiration was defined as a sinusoidal function with a 1-day period, starting from zero at midnight and reaching a maximum rate of 0.5 mm h^{-1} at noon.

Initial conditions assumed dry soil, with water content equal to the wilting point. For groundwater, the initial water table was specified as a flat surface located 1 m below the lake bottom elevation (95 m above the reference datum).

Finally, four monitoring points were located at specific locations over a transect along the x-axis to visualise the impacts on the water table and the lake stage. Thus, point p3 and p4 are close to each other, while p4 is located in the deepest point of the lake (Fig. 4).



285

290

295



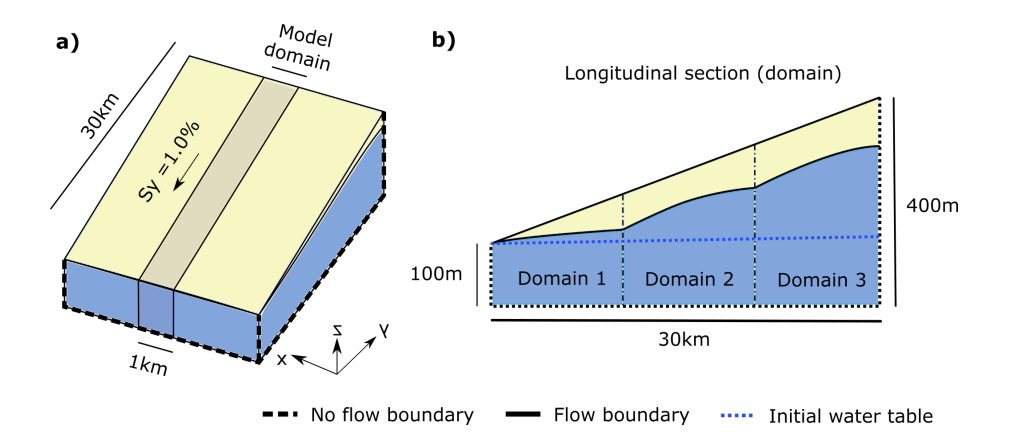


Figure 5. Model domain of synthetic analysis considering different aquifer sub-domains. (a) 3D view of the model indicating the section being modelled, and (b) longitudinal profile indicating the domains for the different transmissivity functions to be applied.

2.3.2 Simulating the effect of multi-transmissivity functions

To illustrate the effect of a groundwater system under the influence of multiple transmissivity functions, we have performed a series of numerical experiments using an idealised aquifer system and uniform precipitation rates over the entire model domain. The model domain consisted of a transect one-dimensional groundwater flow comprising 30 grid cells, each with a resolution of $1 \text{ km} \times 1 \text{ km}$. The model domain was partitioned into three equal sections, with each section assigned a distinct transmissivity function for each simulation (Fig. ??).

Numerical experiments were conducted by changing the transmissivity functions assigned to each section for each simulation. The total number of simulations covered all possible combinations of the three functions. A uniform recharge rate of 0.001 m day⁻¹, a common value for humid areas (Moeck et al., 2020), was applied across the entire domain. All simulations were run until a steady state was reached. Steady-state was assumed to be reached when the change in the water table elevation was less than 1 mm for all cells.

2.4 A regional world example of the Horn of Africa Dryland region

To test the model improvement on the simulation speed, we performed simulations using a large area located in the East Africa Dryland Region (Fig. 6). The modelled area is approximately 2.1 million km^2 and it extends from the Rift Valley in Ethiopia on the west to the Indian Ocean on the east, and, from Mt Kilimanjaro at the south to the Gulf of Aden on the north. The study region covers the whole of Somalia, and Djibouti, most of Kenya and eastern Ethiopia, and a small area in northern Tanzania (Fig. 6). The area is characterised by relatively low relief in most of Somalia, with areas of higher relief in the Ethiopian and Kenyan highlands, where elevations exceed 4000 m. The region is also characterised by a wide range of climatological conditions ranging from hyper-arid to semi-arid climate in Somalia, arid and semi-arid in coastal Kenya, and a savanna to sub-tropical climate in the Ethiopian and Kenyan highlands (CGIAR-CSI, 2009; Peel et al., 2007) (Fig. 6b).





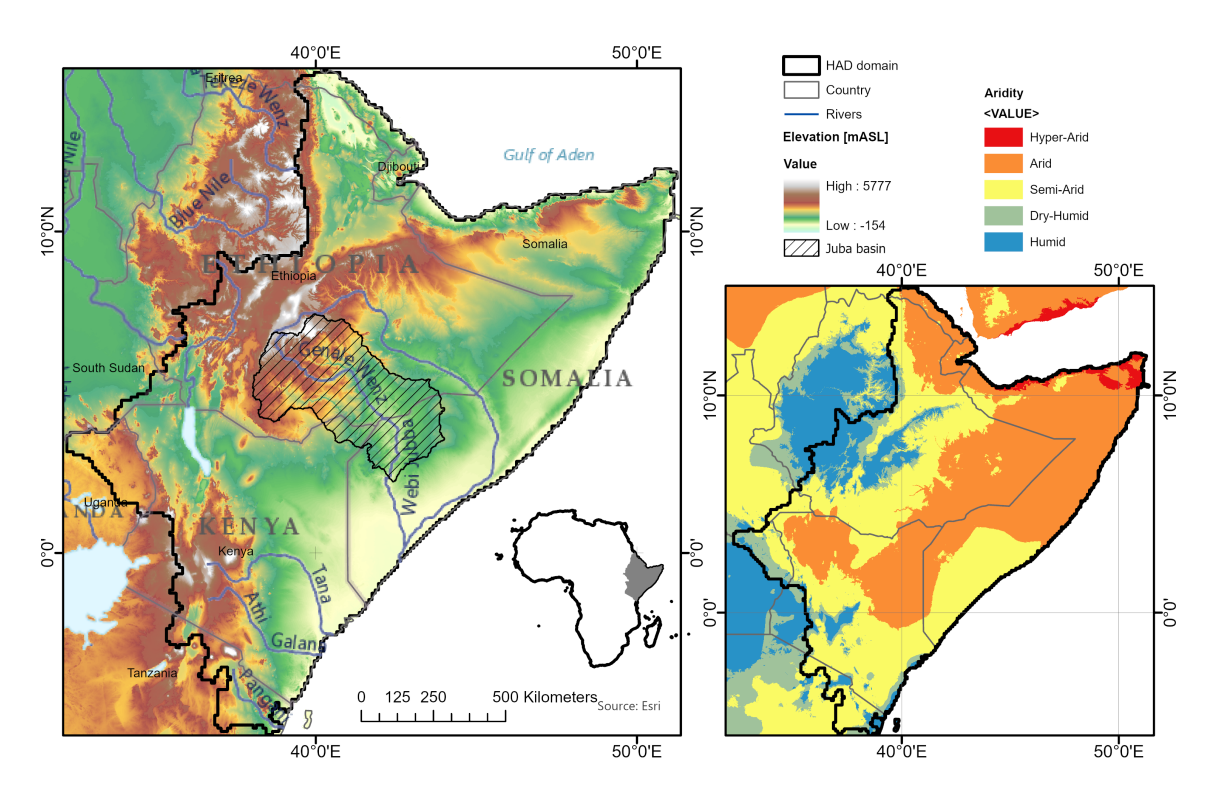


Figure 6. (a) Location and extent of the Horn of Africa Dryland (HAD) region and the model domain. The hatched area represents the Juba Basin. (b) Spatial distribution of climatological zones within the HAD region.

Precipitation varies considerably temporally and spatially across the region. The driest areas in the north, northeast, and the central plateaus have annual totals of up to 300 mm, whereas in humid areas annual precipitation increases up to 1800 mm in the Ethiopian highlands and Mt. Kenya (Cocking et al., 2024). In arid areas, precipitation is delivered in two distinct rainy seasons, a long rainy season which occurs approximately from March to May (MAM) and a short rainy season between approximately October to December (OND). In more humid areas, precipitation is characterised by unimodal distribution (Palmer et al., 2023; Wainwright et al., 2019). The area is dominated by ephemeral streams with only three large perennial rivers across the domain, the Juba and Shabelle in Somalia and the Tana river in Kenya (Messager et al., 2021). In dry areas, the water table is generally deep, reaching values of 400 m depth or even deeper such as the Ogaden area (Godfrey et al., 2019). East African drylands are thought to hold vast groundwater resources which could buffer climate variability ((Idowu et al., 2017; MacDonald et al., 2012; Quiroga et al., 2022; Adloff et al., 2022).

2.4.1 Model parameterisation

300

305

The model was parameterised using datasets available at global and regional scales (Table 1). All datasets were reprojected and aligned to a common UTM projection. For continuous variables, datasets were interpolated using a bilinear approach,





whereas a Nearest Neighbour approach was used for datasets with discrete data. Additionally, datasets provided as polygons (e.g. shapefiles) were rasterised by assigning values from features with the greatest extent within the grid cell.

Table 1. Model parameters, descriptions, units, and data sources.

Parameter	Description	Dimension	Source			
Model doma	Model domain and surface parameters					
z	Digital elevation model	[L]	HydroShed (Linke et al., 2019)			
$h_{ m lake}$	Lake bathymetry	[L]	GLOBathy (Khazaei et al., 2022)			
Overland flo	ow .					
k_T	Recession time for channel streamflow	$[T^{-1}]$	$0.083 h^{-1}*$			
W	Channel width	[L]	10 m			
L_{ch}	Channel length	[L]	Grid size			
K_{ch}	Channel saturated hydraulic conductivity	$[L T^{-1}]$	$10.9~{\rm mm}~{\rm h}^{-1}$			
Unsaturated	zone					
$ heta_{ m wp}$	Water content at wilting point	[-]	AfSoilGrids (Leenaars et al., 2018)			
$ heta_{ m fc}$	Water content at field capacity	[-]	AfSoilGrids (Leenaars et al., 2018)			
$ heta_{ m sat}$	Saturated water content	[-]	AfSoilGrids (Leenaars et al., 2018)			
ψ	Suction head	[L]	Dai et al. (2019)			
λ	Soil pore size distribution	[-]	Dai et al. (2019)			
K_{sat}	Saturated hydraulic conductivity	$[L T^{-1}]$	Dai et al. (2019)			
D	Rooting depth	[L]	AfSoilGrids (Leenaars et al., 2018)			
Saturated Zone						
S_y	Specific yield	[-]	GLHYMPS (Gleeson et al., 2014)			
$K_{ m aq}$	Aquifer saturated hydraulic conductivity	$[LT^{-1}]$	GLHYMPS (Gleeson et al., 2014)			
f_D	Effective aquifer depth (for exponential function)	[L]	60 m			

2.4.2 Forcing and evaluation datasets

310

The model was forced with the global gridded rainfall from IMERG (Huffman et al., 2015) and potential evapotranspiration from hPET (Singer et al., 2021). These datasets were chosen due to their high spatial and temporal resolutions, 0.1° and 30 min for IMERG, and 0.1° and 1 hr for hPET.

The model was not calibrated, as this was not the main goal of the manuscript. However, selected model outputs were compared with available remote sensing products to provide an initial assessment of the model's potential performance. Specifically, soil moisture was compared with the combined passive and active soil moisture product from the European Space Agency (ESA CCI) (Dorigo et al., 2017), actual evapotranspiration was compared with the Global Land Evaporation Amsterdam Model (GLEAM) product (Martens et al., 2017), and total water storage anomalies were compared with data from the Gravity Recovery and Climate Experiment (GRACE) (Save et al., 2016). Pearson's correlation analysis was performed for the



325

330

335

340

345

350



three model outputs. Time series of these variables, along with the corresponding remote sensing products, were also plotted for visual evaluation in the Juba Basin. Finally, to enable comparison between observed and simulated soil moisture time series, both were scaled between 0 and 1. This normalization allowed comparison between the shallow (2-5 cm) soil water content represented by the ESA CCI product and the bucket-model approach used in DRYP 2.0 (Quichimbo et al., 2023; Brocca et al., 2017).

2.4.3 Model settings and initial conditions

The model time step was specified as 1 h and the spatial resolution as 1 km. The regional simulation used the Philip's infiltration approach for precipitation partitioning and the exponential transmissivity approach for the groundwater component. The simulation was run for a 23-year period, from 01/07/2000 to 31/12/2022. The initial date was chosen based on availability of IMERG precipitation data. Initial conditions were specified after running the model four times over a period of 20 years, with the first simulation starting at dry conditions for soil storage and global water table depth (Fan et al., 2013) for groundwater.

3 Results

3.1 Groundwater-lake interactions

Figure 7 illustrates the interactions between groundwater and the lake within the model domain. The figure displays selected time periods to demonstrate the variability of the forcing dataset including the wet period when precipitation occurred and the dry period (Fig. 7a), as well as the period between lake emergence and the onset of dynamic steady-state conditions in groundwater–lake interactions (Fig. 7b). Note that the dates shown are used only as temporal references along the time axis.

Figure 7b shows how the water table varies over time at several monitoring points as a response to temporal changes in recharge. It can be observed that at points located within the lake (p3 and p4), the rise in the water table differs significantly from that at points located outside the lake (p1 and p2). Notably, the water table at point p3 reaches an almost constant level earlier (at time t-2), indicating that the water table has reached the surface elevation. This suggests that groundwater discharge to the surface occurs at this location, ultimately contributing to lake inflow. In contrast, points p1, p2, and p4 take a longer time to reach dynamic steady-state conditions, which is nearly achieved at time t-4. At point p1, the water table does not reach either the root zone or the surface, resulting in higher fluctuations compared to the other points. The slower response at p4, compared to the other locations, is primarily due to differences in storage capacity between the lake (S = 1.0) and the aquifer ($S_y = 0.01$).

The lake receives lateral inflow from the aquifer, runoff due to saturation excess from non-flooded cells, and direct precipitation. It loses water through direct evaporation from the lake surface. Figures 7a and 7b show transects of the water table along the x- and y-axes, respectively, across the centre of the model domain (see Fig. 4). These figures show the effects of the dynamics of these fluxes on groundwater heads. As the water table rises and intersects the lake bottom elevation, the high storage capacity of the lake significantly influences the rate of water level change. This transition effectively converts the lake





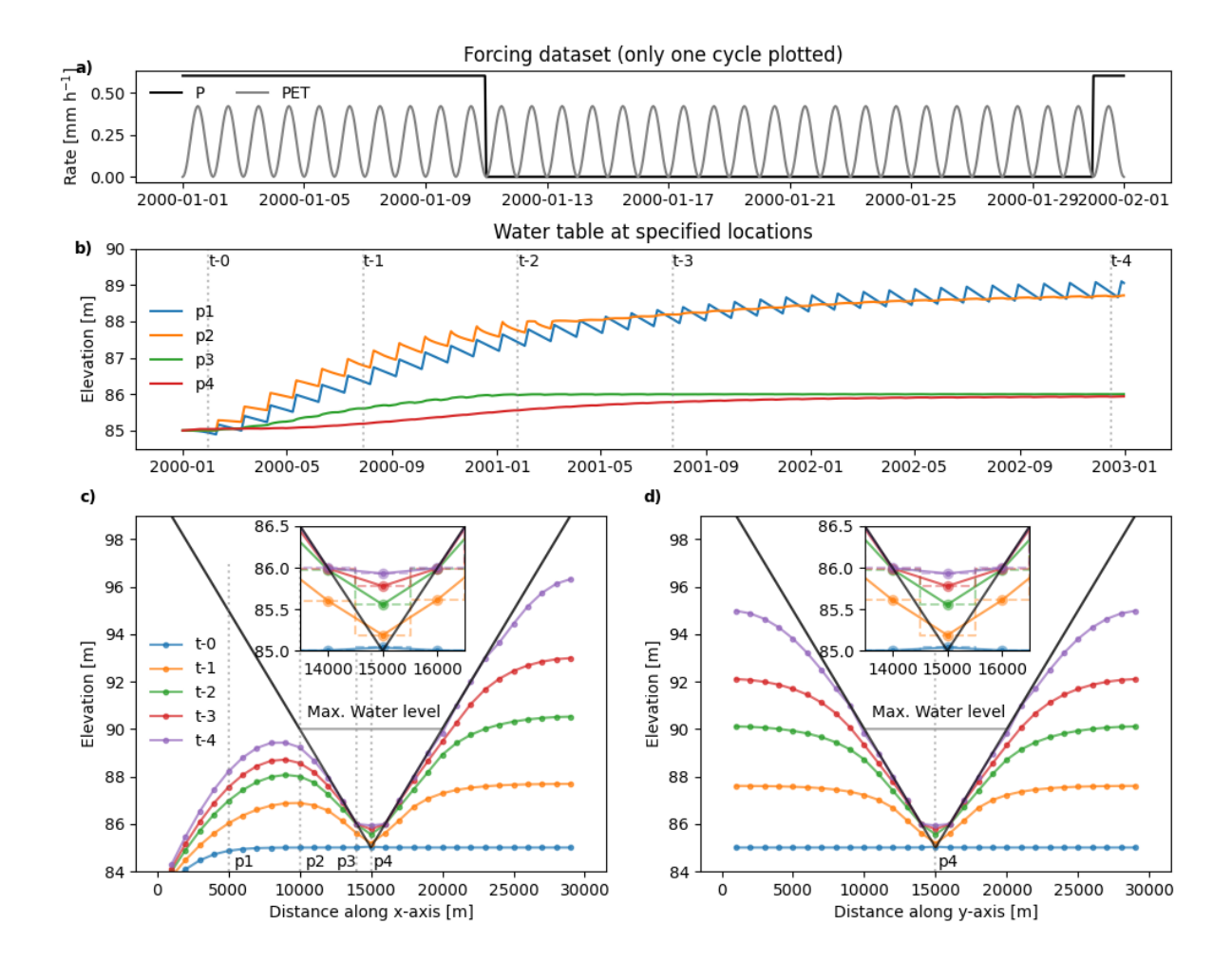


Figure 7. Example simulation of groundwater-lake interactions (GW-LKS) component, (a) time series showing one cycle of forcing datasets of P and PET; (b) water table fluctuations at specific locations over a selected period (see Fig. 4c for location of monitoring points); (c) shows the cross sections of the simulations along the x-axis showing the effect of the constant head boundary condition; and (d) cross section along the y-axis. Insect figures correspond to the lowest point of the lake for each corresponding panel.

into a variable-head boundary condition. From the time the lake starts storing water, the water exchange between the lake and the aquifer is governed by the hydraulic gradient between the water table and the lake stage. At point p4 (see Figs. 7c and d), which represents the deepest part of the lake, the water table rises more gradually until it reaches the elevation of point p3. In order to further increase the lake stage, all cells need to be flooded; however, at this point, the system has already reached dynamic steady state, therefore, no further increase is expected in the model.



360

365

380

385



3.2 Simulating the effect of multi-transmissivity functions

Figure 8 illustrates the impact of using different transmissivity functions within the same model domain on water-table elevation. The figure presents results from a series of simulations that permutate the three transmissivity functions implemented in the model: constant (C), linear (L), and exponential (E)—as shown in Fig. 3. All simulations reached a steady state after a 10-year simulation period.

The results reveal significant variability in water-table elevations across all scenarios (Fig. 8). The influence of each transmissivity function depends strongly on its spatial position within the model domain. For instance, when the exponential function (E) is applied, the water table remains close to the surface throughout its spatial extent. In contrast, the linear and constant functions exhibit greater depth variations, particularly with increasing distance from the constant-head boundary. This behaviour is expected as the exponential function leads to a rapid reduction in transmissivity with water table depth, limiting downward water movement.

Furthermore, the exponential function can exert a controlling effect on adjacent aquifer zones. When located in the lower part of the domain, the exponential zone behaves similarly to a head-like boundary condition for overlying aquifers (e.g., model configurations L–E–C and C–E–L in Fig. 8). Conversely, when positioned in the upper domain, the lower aquifer zones may act as flux-like boundary conditions, modulating flow into the exponential zone (e.g., L–C–E and C–L–E scenarios).

This synthetic analysis demonstrates that spatial variability in aquifer transmissivity can have a substantial effect on watertable configuration and, consequently, on the broader water balance. This model capability is particularly relevant in real-world systems, where geological, tectonic, and weathering processes often give rise to spatially heterogeneous transmissivity. Incorporating such heterogeneity—even within a single-layer domain—can support the development of more realistic groundwater models as well as an enhanced representation of stream network connectivity (Abhervé et al., 2025).

3.3 Regional model simulation

Model simulations at the regional scale showed a significant improvement in computational efficiency. This new version of the model reduced simulation time by a factor of 40 compared to the original DRYP 1.0. For instance, the regional simulation, consisting of 6 million cells, required one hour of wall-clock time to simulate a 30-day period (hourly time steps). This enhancement greatly expands the potential for applying the model to regional and continental scales, as well as for integration into seasonal water forecasting systems (Daron et al., 2025).

Below, we briefly describe the model outputs at regional scales. As the model results are uncalibrated, performance evaluation is limited to visual inspection and correlation analysis. Future research will focus on model calibration and a more detailed analysis of hydrological processes and their controlling factors.

Figure 9 presents the spatial correlation between model outputs and remote sensing datasets for three key variables: actual evapotranspiration (AET), soil moisture (SM), and total water storage anomalies (TWSA). Overall, the model demonstrates good performance across all variables. The strongest performance is observed for AET (Fig. 9b), with correlation coefficients exceeding 0.8 across most of the model domain. Negative correlations are limited to small areas, particularly in the highlands





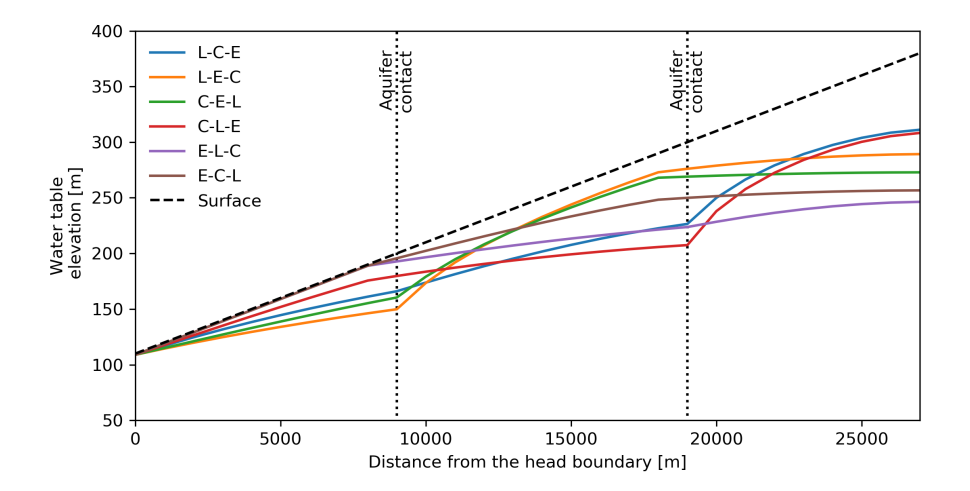


Figure 8. Steady-state water table elevations after a 10-year simulation for different permutations of the three transmissivity functions implemented in the model: L = linear, C = constant, and E = exponential (see Fig. 3).

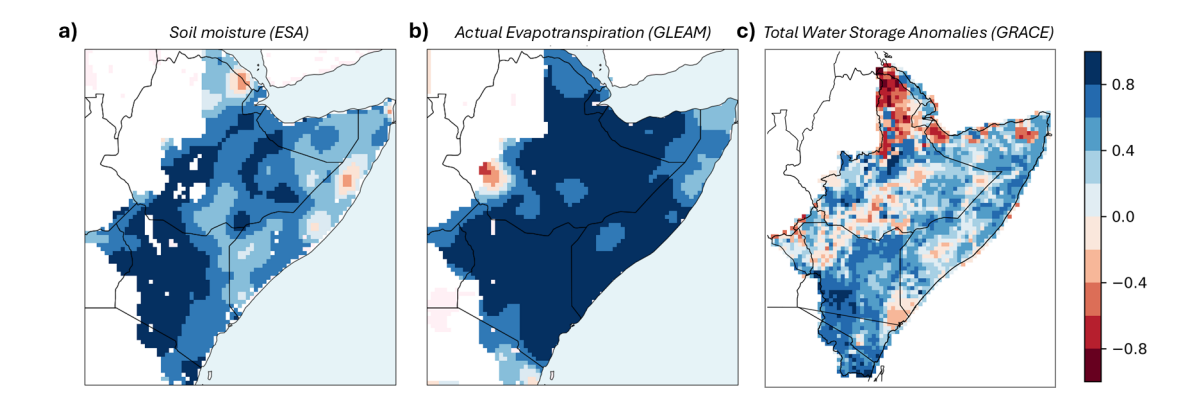


Figure 9. Spatial correlation between model outputs and remote sensing datasets for (a) scaled soil moisture (θ , ESA CCI), (b) actual evapotranspiration (AET, GLEAM), and (c) total water storage anomalies (Δ TWSA, GRACE-TWSA).

of western Ethiopia. Soil moisture also exhibits high correlations, with values exceeding 0.8 primarily in the southwestern part of the domain, especially in western Kenya. TWSA shows predominantly positive correlations across the domain; however, negative correlations are observed in the northern region and in isolated areas.

These results highlight the model's capability to represent hydrological fluxes and states that are essential for closing the water balance over large spatial domains. Given the scope of the current study, analysis is limited to correlation metrics. However, future work will investigate the dependence of hydrological fluxes on climate and geomorphological conditions.





405

410

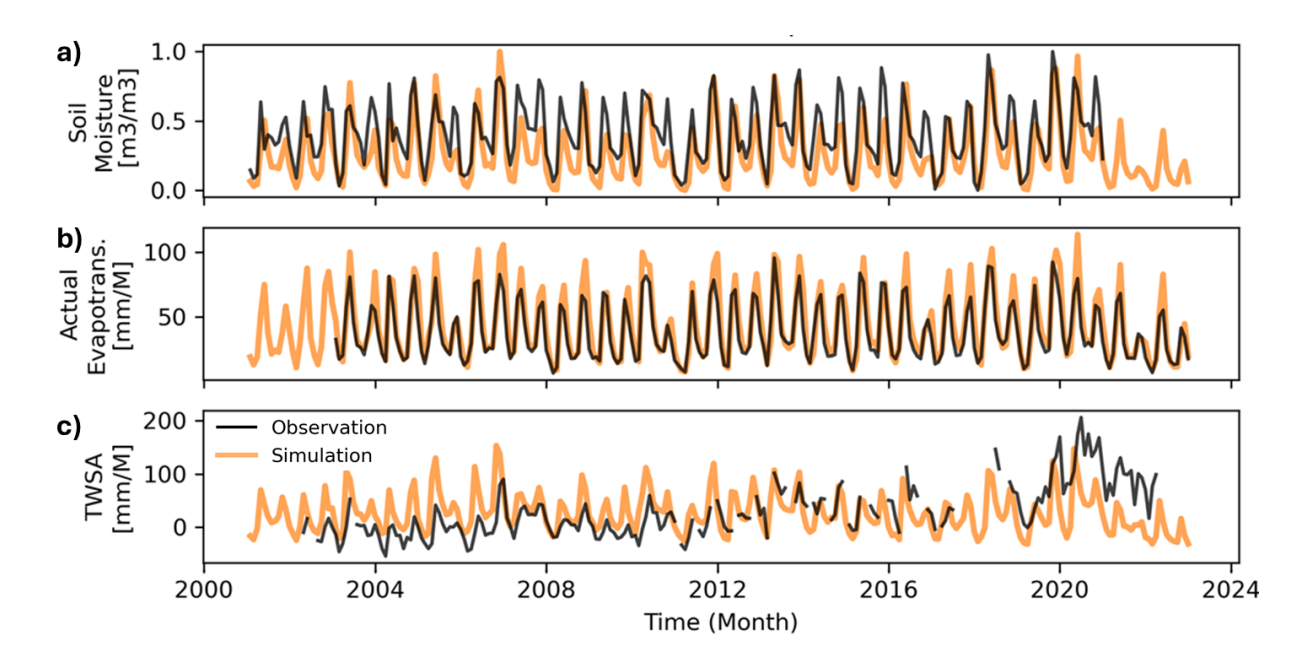


Figure 10. Comparison between modelled and remote sensing data (shown in parentheses) for the temporal evolution of water fluxes and states in the Juba Basin (see Fig. 6a), extracted from the regional simulation: (a) actual evapotranspiration (GLEAM), (b) scaled soil moisture (ESA CCI), and (c) total water storage anomalies (GRACE TWSA).

Accurate representation of these fluxes, particularly when combined with additional observations, may help reduce uncertainty in poorly constrained components of the water cycle, such as groundwater recharge.

It is also important to emphasize that outputs at the regional scale can provide significant insights at the catchment scale. To illustrate this, model results were analyzed at the basin scale using the Juba basin (200,000 km²), located in Ethiopia (Fig. 6a). Figure 10 shows the temporal evolution of model outputs in comparison to remote sensing datasets for AET, SM, and TWSA. Overall, the simulated AET aligns well with GLEAM AET estimates, capturing both magnitude and seasonal variability. Similarly, the soil moisture simulation exhibits good agreement with ESA-CCI data, effectively representing monthly variability. The model also captures the temporal dynamics of TWSA, with many peak values matching those in the GRACE-based record. However, a slightly negative trend in simulated TWSA contrasts with the weak positive trend observed in GRACE data. Furthermore, the model tends to overestimate TWSA during the first half of the simulation period and underestimate it during the second half, especially between 2019 and 2022. These discrepancies could be addressed through calibration in future work.

Overall, the outputs from the uncalibrated model demonstrate its potential to simulate consistent hydrological fluxes at both regional and basin scales. The high spatial resolution enables the representation of hydrological processes across diverse climatological and geomorphological environments. This has the potential to enhance our understanding and quantification of water partitioning. Accurate simulation of water fluxes and states is essential for assessing the impacts of climate variability on water resource availability, as well as their implications for ecosystems and human communities.



415

420



4 Conclusions

A new version of the parsimonious hydrological model DRYP (Dryland water Partitioning model) has been developed. This enhanced version improves the model's capability to simulate processes at regional scales. It is computationally more efficient than the previous version, enabling simulations over larger spatial domains. New process representations have been introduced, which are crucial under diverse and contrasting climatological conditions. These include groundwater–lake interactions, spatially variable aquifer systems, interception and canopy evaporation, and the inclusion of ponds and shallow water stores.

This study demonstrates the model's performance under two idealised scenarios: (i) groundwater-lake interactions (GW-LKS) and (ii) a spatially variable aquifer system. In the GW-LKS scenario, the model captures the role of lake stage as a variable-head boundary condition, which governs the exchange of water between the aquifer and the lake. In the spatially variable aquifer system scenario, the model simulates the impact of varying transmissivity functions on water table dynamics—a key feature when representing spatially heterogeneous lithologies and complex topography. These model capabilities provide a foundation for improved representation of long-term hydrological responses to both climate variability and anthropogenic influences.

The model's numerical performance was further evaluated over a large-scale domain in the Horn of Africa Drylands (HAD). The optimised flow routing scheme significantly enhances computational efficiency, reducing simulation time by a factor of 40. Even without prior calibration, the initial simulation results show the model's capacity to represent key hydrological fluxes across the domain. Comparisons with remote sensing datasets indicate generally good agreement for soil moisture (ESA), actual evaporation (GLEAM), and total water storage anomalies (GRACE-TWSA).

Overall, the new version of our model, DRYP 2.0, provides an efficient tool for estimating water partitioning at regional to continental scales. While further improvements—such as the parallelisation of computationally intensive components like flow routing—are planned, the current version already expands the model's applicability for assessing water resource availability under the combined pressures of climate variability and human activity, and enhances its potential integration into seasonal water forecasting systems.

35 Appendix A: Appendix

A1 List of variables and model parameters

Table A1: Model parameters, their descriptions, and dimensions. A detailed description of all parameters is found in section 2 and Quichimbo et al. (2021)

Parameter	Description	Dimension
\overline{AET}	Actual evapotranspiration	$[L T^{-1}]$
AET_{SZ}	Capillary rise	$[\mathrm{L}\mathrm{T}^{-1}]$
		Continued on next page





Parameter	Description	Dimension
В	Initial suction head	[L]
C	River conductivity	$[L^2T^{-1}]$
c	Readily available water factor	[-]
$D_{ m root}$	Rooting depth	[L]
$D_{ m uz}$	Unsaturated zone thickness	[L]
ET_0	Reference evapotranspiration	$[\mathrm{L}\mathrm{T}^{-1}]$
f	Infiltration rate	$[L T^{-1}]$
f*	Vegetation type factor	[-]
f_D	Effective aquifer depth (exponential function)	[L]
h	Water table elevation	[L]
h_b	Aquifer bottom elevation	[L]
$h_{ m riv}$	River stage elevation	[L]
I	Cumulative infiltration	[L]
I_c	Cumulative infiltration capacity	[L]
i_{ch}	Channel losses	$[L^3 T^{-1}]$
K_c	Crop coefficient	[-]
$K_{ m aq}$	Aquifer saturated hydraulic conductivity	$[L T^{-1}]$
K_{ch}	Channel saturated hydraulic conductivity	$[L T^{-1}]$
k_{dt}	Schaake reference parameter	[-]
$K_{dt,\mathrm{ref}}$	Reference hydraulic conductivity	$[L T^{-1}]$
K_{sat}	Saturated hydraulic conductivity	$[L T^{-1}]$
k_T	Recession time for channel streamflow	$[T^{-1}]$
$L_{ m ch}$	Channel length	[L]
P	Precipitation	[L]
p	Precipitation rate	$[L T^{-1}]$
PET_{SZ}	Max water uptake from saturated zone	$[L T^{-1}]$
PET	Potential evapotranspiration	$[L T^{-1}]$
q_0	Initial volumetric flow rate	$[L^3 T^{-1}]$
$Q_{ m ASW}$	Surface water abstraction	$[L^3 T^{-1}]$
$Q_{ m ASZ}$	Groundwater abstraction	$[L^3 T^{-1}]$
$Q_{ m APND}$	Pond abstractions	$[L^3 T^{-1}]$
Q_{in}	Channel inflow	$[L^3 T^{-1}]$
$q_{ m in}$	Volumetric flow entering stream cell	$[L^3 T^{-1}]$
		Continued on next page





Parameter	Description	Dimension
$Q_{ m out}$	Channel outflow	[L ³]
$q_{ m rir}$	Saturation excess overland flow	$[L T^{-1}]$
q_s	Groundwater discharge into streams	$[L T^{-1}]$
Q_{TL}	Transmission losses	$[L^3]$
R	Groundwater recharge	$[L T^{-1}]$
r	Regularisation factor	[-]
S_p	Sorptivity	$[L^2T^{1/2}]$
S_{SW}	Channel storage	$[L^3]$
S_{SZ}	Storage in the saturated zone	[L]
S_{UZ}	Storage in the unsaturated zone	[L]
S_y	Specific yield	[-]
T	Aquifer transmissivity	$[L^2 T^{-1}]$
TAW	Total available water for evapotranspiration	[L]
W	Channel width	[L]
z	Surface elevation	[L]
$z_{ m riv}$	Bottom channel elevation	[L]
β	Water stress coefficient	[-]
$ heta_{ m fc}$	Water content at field capacity	[-]
$ heta_{ m sat}$	Saturated water content	[-]
$ heta_{ m wp}$	Water content at wilting point	[-]
λ	Soil pore size distribution	[-]
μ_Y	Log mean of saturated hydraulic conductivity	$[L T^{-1}]$
σ_Y	Std. dev. of log saturated hydraulic cond.	$[L T^{-1}]$
ψ_a	Initial suction head	[L]
ψ_f	Suction head	[L]

A2 Groundwater - Lake interaction

A2.1 Implementation

To avoid numerical instabilities at the groundwater–lake interface, a regularisation approach was implemented by applying a smooth transition between a flux boundary condition and a constant head boundary, using a convex function following Marçais et al. (2017):

$$q_{\rm lk} = f_u \left(\frac{h - h_b}{z - h_b}\right) f_g \left(\nabla \cdot \left(-K_{\rm aq} h \nabla h\right) + R - E_{\rm SZ} - \frac{Q_{\rm ASZ}}{A_{\rm lks}} - q_{\rm riv}\right) \tag{A1}$$





where: h is the hydraulic head [L], h_b is the aquifer bottom elevation [L], f_g is the Heaviside step function, K_{aq} is the saturated hydraulic conductivity tensor [L T⁻¹], R is recharge [L T⁻¹], q_{riv} is the river flux [L T⁻¹], Q_{ASZ} is lake abstractions [L³ T⁻¹], A_{lks} surface area [L²], and f_u is a continuous regularization function ranging between 0 and 1, given by:

$$f_u = \exp\left(-\frac{1-u}{r}\right),\tag{A2}$$

where: r is a dimensionless regularization factor (r > 0), set to 0.001 as in Marçais et al. (2017).

Change in lake storage is handled through a variable-depth lake storage components. The thickness of the lake storage ($D_{\rm lks}$) is defined as:

$$450 \quad D_{\text{lks}} = \min \left[D_{\text{bathy}}, h - z_{\text{bathy}} \right] \tag{A3}$$

where: D_{bathy} is the lake bathymetry [L], z_{bathy} is the lake bottom elevation [L], and h is the groundwater table elevation/lake stage [L].

When the water table is below the z_{bathy} , there is no groundwater-lake interaction. However, when the water table rises above z_{bathy} due to recharge or lateral groundwater flow, two-way interaction is activated, and the water table is updated based on the change in saturated zone storage:

$$\frac{\Delta S_{\rm SZ}}{\Delta t} = \nabla \cdot (-K_{\rm aq} h \nabla h) + R - Q_{\rm ASZ} \tag{A4}$$

where $\Delta S_{\rm SZ}$ is the change in saturated zone storage per unit area [L³ L⁻²], and $Q_{\rm ASZ}$ is groundwater abstraction [L T⁻¹].

(i) Rising water table crossing z_{bathy} :

Water Table Update Scenarios

460
$$h_t = [\Delta S_{SZ} - (z_{bathy} - h_{t-1})S_y] + z_{bathy}$$
 (A5)

(ii) Falling water table crossing z_{root} :

$$h_t = -\frac{1}{S_y} \left[\Delta S_{\text{SZ}} - (h_{t-1} - z_{\text{bathy}}) \right] + z_{\text{bathy}}$$
(A6)

(iii) Water table above z_{bathy} :

$$h_t = \Delta S_{SZ} + h_{t-1} \tag{A7}$$

465 (iv) Water table below z_{bathy} :

$$h_t = \frac{\Delta S_{\rm SZ}}{S_u} + h_{t-1} \tag{A8}$$

A3 Ponds and Shallow water bodies

From Equation 10, assuming that precipitation, runoff, and abstraction immediately increase or decrease the volume of water in the pond, and that any excess water from the pond is instantaneously removed, the change in pond storage due to evaporation from the surface can be estimated as follows:

$$\frac{dV}{dt} = -AE_{pnd},\tag{A9}$$





where A [L²] is the surface area of the pond, assumed to be circular, with the radius depending on the pond water stage , h [L], such that $r = b^*h^a$. Thus, A can be expressed as:

$$A = \pi \left(b^* h^a\right)^2 = \pi b h^{2a},\tag{A10}$$

where a and b are dimensionless parameters that control the shape and extent of the pond, respectively. Note that b is b^{*2} . The change in pond volume due to a change in water stage is given by:

$$\frac{dV}{dh} = \pi \left(b^* h^a\right)^2. \tag{A11}$$

The volume of water stored in the pond at any given stage can be estimated by integrating Equation A11. Solving this expression for h, and assuming that V(h = 0) = 0, yields the following relationship between volume and stage:

480
$$h = \left[\frac{2a+1}{\pi b}V\right]^{\frac{1}{2a+1}}$$
 (A12)

Substituting the pond stage from Equation A12 into Equation A10, and then into Equation A9, and solving the resulting first-order differential equation for V, assuming $V(t=0) = V_0$ and $V(t=\Delta t) = V$, gives the following analytical solution:

$$V = \left[V_0^{\frac{1}{2a+1}} - \frac{\pi b E}{2a+1} \left(\frac{2a+1}{\pi b} \right)^{\frac{2a}{2a+1}} \Delta t \right]^{2a+1}. \tag{A13}$$

Equation A13 contains two unknown parameters, a and b. The solution is non-trivial and can be estimated using observations of stage, maximum depth (h_{max}) , maximum extent (A_{max}) , and maximum volume (V_{max}) of the pond.

Here, it is assumed that the parameters a, h_{max} , and A_{max} are known. Therefore, the parameter b can be computed as:

$$b = \frac{A_{\text{max}}}{\pi h_{\text{max}}^{2a}}.\tag{A14}$$

 $A_{\rm max}$ can be derived from post-processed remote sensing products, such as the Normalized Difference Water Index (NDWI), and $h_{\rm max}$ from high-resolution Digital Elevation Models (DEMs), such as SRTM.

The maximum storage capacity of the pond, V_{max} , is then obtained by solving Equation A13 for V:

$$V_{\text{max}} = h_{\text{max}}^{2a+1} \frac{\pi b}{2a+1}.$$
 (A15)

A4 Simulation of vegetation interception

A4.1 Simulation settings

To illustrate the effect of vegetation interception on precipitation reaching the land surface, we developed a synthetic numerical experiment using precipitation, potential evapotranspiration (PET), leaf area index (LAI), and crop coefficient (k_c) as forcings.

Precipitation events were generated randomly at an hourly time step, without seasonality. Event durations followed a Poisson distribution:

$$P(K=k) = \frac{\lambda^k e^{-\lambda}}{k!}, \quad k = 0, 1, 2, \dots$$
 (A16)





where K is a random variable for event duration [h], λ is the expected event duration (mean), and P(K = k) is the probability of an event lasting exactly k hours.

Storm intensity was represented by a Gaussian distribution:

$$I(t) = I_{\text{max}} \exp\left(-\frac{1}{2} \left(\frac{t-\mu}{\sigma}\right)^2\right) \tag{A17}$$

where I(t) is rainfall intensity [mm h⁻¹] at time t, I_{\max} is peak intensity [mm h⁻¹], μ is the storm center (hours from start), and σ controls storm spread (duration). This yields a smooth storm profile peaking at $t = \mu$.

PET was generated using a sinusoidal function with a 24-hour period, peaking at noon, with a maximum rate of 0.1 mm h⁻¹ (Fig. A1d). Synthetic values of LAI and k_c , typical of temperate maize crops, were prescribed with planting in spring, peak in mid-summer, and senescence in autumn. The model domain was defined as a single grid cell, including only the vegetation and surface water components. Initial conditions were set to dry, with canopy storage assumed to be zero.

A4.2 Simulation results

Figure A1 presents the temporal variation of forcings and canopy-interception outputs. Panels (a–d) show forcings at monthly (left) and hourly (right) scales.

Model results demonstrate that interception increases with LAI (Fig. A1e), reflecting larger canopy storage capacity and higher canopy evaporation (Fig. A1g). During rainfall events, canopy evaporation follows the PET signal, provided sufficient water is available in canopy storage (Fig. A1f). Storage reaches its maximum capacity depending on precipitation intensity; excess precipitation then becomes throughfall. Interception is therefore the sum of canopy storage and canopy evaporation.

A5 Simulation of shallow ponds

A5.1 Simulation settings

515

520

525

To illustrate the emergence and dry-up of shallow ponds, as well as the temporal variation of their water balance, we developed a synthetic example. The model domain consisted of three cells, each containing one pond. All ponds had the same maximum surface area ($A_{max} = 225 \text{ m}^2$, r = 8.5 m) and maximum depth (h = 4 m). However, the shape parameter a, which controls the relationship between pond stage and surface area, was varied across the three cases (a = 0.25, 0.50, 0.75; Fig. A2a-c). These values were selected to illustrate how pond shape influences water balance dynamics. The model included only the surface water component, as shallow ponds interact exclusively with surface processes; groundwater interactions were not represented.

The simulation was forced with synthetic precipitation and potential evapotranspiration (PET). Precipitation was generated using a rectangular step function, producing an event of 1 mm h^{-1} for 10 days, followed by a 15-day dry spell. PET was represented by a sinusoidal function with a 1-day period and a maximum rate of 10 mm h^{-1} (Fig. A2d) to quickly dry up the pond. To capture pond emergence, initial storage was set to zero. The simulation was run for two years.





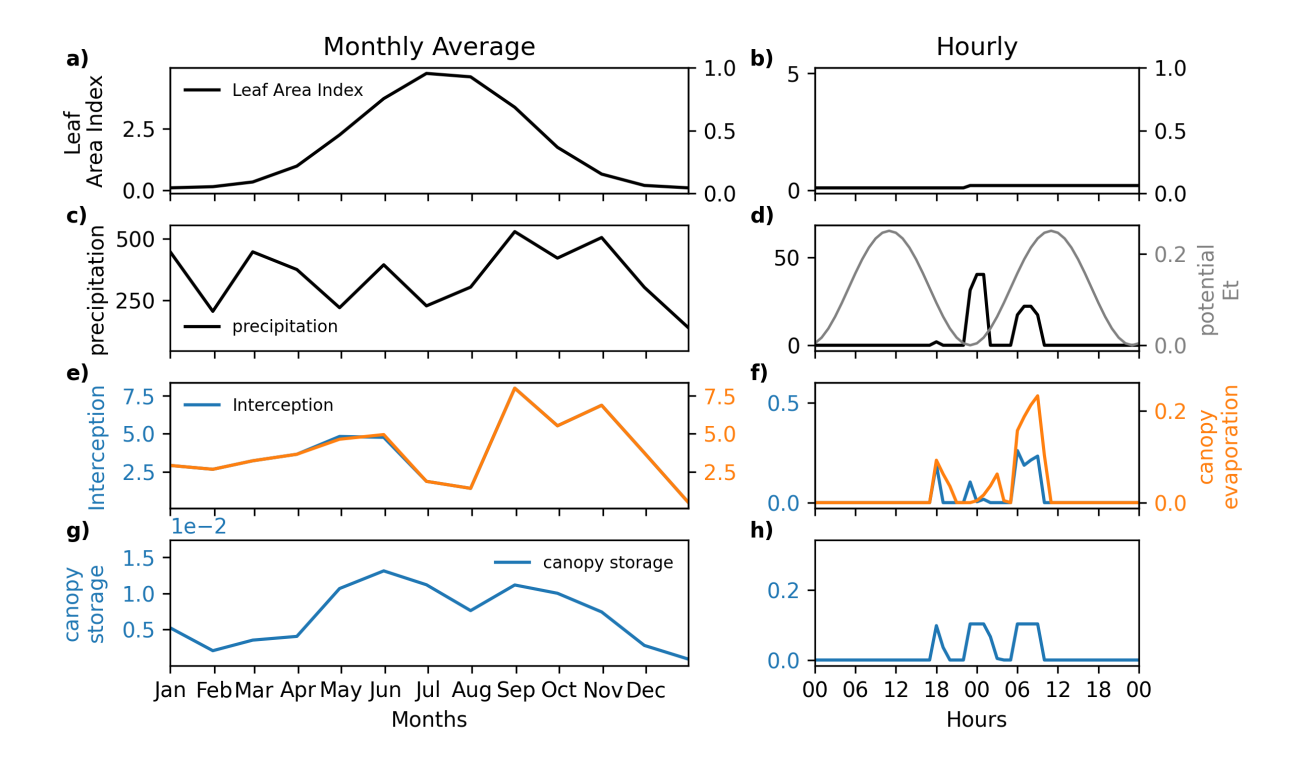


Figure A1. Example simulation of the canopy-interception component. Left panels show monthly data; right panels show hourly data for a selected precipitation event. Black/gray lines represent forcings; colored lines represent model outputs. Panels: (a-b) Leaf Area Index (LAI) and crop coefficient (k_c); (c-d) precipitation (left axis) and PET (right axis in panel d); (e-f) interception (left axis) and canopy evaporation (right axis); (g-h) canopy storage.

A5.2 Simulation results

530

535

Figure A2 shows the simulated storage dynamics for the three specified values of a. Panels a–c illustrate the relationships of pond stage with radius, area, and volume, respectively. Higher values of a lead to smaller changes in radius with stage, whereas lower values produce an exponential relationship. The surface area exhibits a convex shape for a > 0.5 and a concave shape for a < 0.5. As expected, variation in a strongly affects pond volume, with lower values yielding larger storage capacities.

The temporal dynamics of stage, area, and volume also vary with pond shape. Under the same forcing conditions, ponds with low a values take longer to reach maximum stage, since a larger volume is required to fill them (Fig. A2e). Water level decline is similar across scenarios, as it is controlled primarily by evaporation acting at the same rate. Consequently, the decrease in stage is nearly linear. Surface area changes more rapidly for lower a values during the filling phase, while during the drying phase the rate of decrease is less sensitive to a (Fig. A2f).

Pond volume increases linearly during rainfall events for all scenarios (Fig. A2g), reflecting the constant inflow rate (precipitation multiplied by the contributing area, i.e., the cell size). In contrast, drying is nonlinear and varies with pond shape. Ponds



545



540 with low *a* values exhibit faster volume losses, consistent with the fact that evaporation is proportional to surface area, which decreases more slowly with stage in these cases.

Code and data availability. The DRYP 2.0 code is archived at https://doi.org/10.5281/zenodo.17451148 (Quichimbo et al., 2025) and available at https://github.com/AndresQuichimbo/CUWALID/tree/main/cuwalid/dryp (last access: 29 September 2025). Our dataset contains modified Copernicus Climate Change Service information (1981–present) available at https://cds.climate.copernicus.eu/datasets/reanalysis-era5-land?tab=download (European Centre for Medium-Range Weather Forecasts, 2018). IMERG Precipitation datasets are publicly available at https://gpm.nasa.gov/data/directory (last accessed: 20/02/2025). hPET datasets are publicly available at https://doi.org/10.5523/bris.qb8ujazzda0s2aykkv0oq0ctp (last accessed: 01/02/2027); ESA-European Space Agency datasets are publicly available at https://www.esa-soilmoisture-cci.org/ (last accessed: 15/02/2025); GRACE: Gravity Recovery And Climate Experiment datasets are publicly available at http://grace.jpl.nasa.gov (last accessed: 20/02/2025).

550 *Author contributions.* EAQ, MOC, MBS, and KS conceptualised the study and performed data analysis. EAQ wrote the code. EAQ wrote the original draft of the paper, with further contributions from all co-authors. MOC and MBS provided supervision.

Competing interests. The contact author has declared that neither they nor their co-authors have any competing interests.

Disclaimer. Any use of trade, firm, or product names is for descriptive purposes only and does not imply endorsement by Cardiff University.

Publisher's note: Copernicus Publications remains neutral with regard to jurisdictional claims in published maps and institutional affiliations.

555 tions.

Acknowledgements.

560

Financial support. E. Andrés Quichimbo received financial support fromEuropean Commission Horizon 2020 Postdoctoral Fellowships - Marie Skłodowska-Curie ("HYDROAWARE AFRICA", grant no 101209082) and UKRI-EPSRC-Strategic Impact Funding. Mark O. Cuthbert gratefully acknowledges funding for an Independent Research Fellowship from the UK Natural Environment Research Council (grant no. NE-P017819-1). Michael Bliss Singer has been supported by the U.S. National Science Foundation (grant nos. BCS-1660490 and EAR-1700517) and the U.S. Department of Defense's Strategic Environmental Research and Development Program (grant no. RC18-1006). The team has been supported by the Global Challenges Research Fund (GCRF; "Impacts of Climate Change on the Water Balance in East African Drylands"), The Royal Society ("DRIER", grant no. CHL-R1-180485), and the European Union's Horizon 2020 programme ("DOWN2EARTH", grant no. 869550).





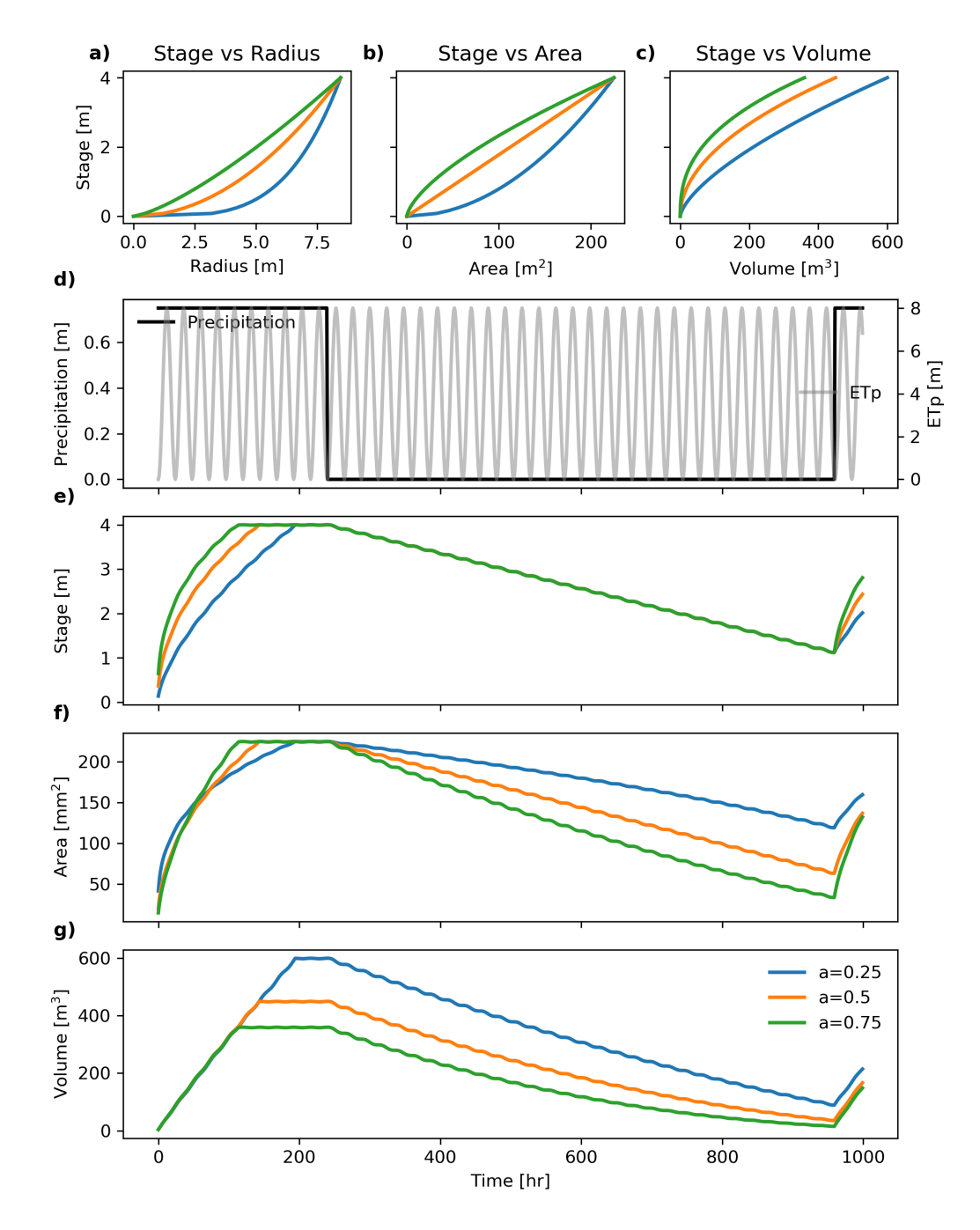


Figure A2. Example of shallow pond water balance simulations for three pond shape parameters (a = 0.25, 0.50, 0.75) using DRYP 2.0. Panels (a–c) show geometric relationships between pond stage and radius, surface area, and volume, respectively. Panel (d) shows the forcing data, (e) shows the temporal evolution of pond stage, (f) shows changes in surface area over time, and (g) shows the variation of pond storage over time.





565 References

595

600

- Abhervé, R., Roques, C., de Dreuzy, J.-R., Van Der Veen, T., Dumaine, L., Chatton, E., Brunner, P., Aquilina, L., and Servière, L.: Projected Climate Change Impacts on Groundwater–Surface Water Connectivity in a Compartmentalized Mountain Headwater Bedrock Aquifer, Water Resources Research, 61, e2025WR040083, https://doi.org/10.1029/2025WR040083, _eprint: https://agupubs.onlinelibrary.wiley.com/doi/pdf/10.1029/2025WR040083, 2025.
- Adloff, M., Singer, M. B., MacLeod, D. A., Michaelides, K., Mehrnegar, N., Hansford, E., Funk, C., and Mitchell, D.: Sustained Water Storage in Horn of Africa Drylands Dominated by Seasonal Rainfall Extremes, 49, e2022GL099299, https://doi.org/10.1029/2022GL099299, eprint: https://onlinelibrary.wiley.com/doi/pdf/10.1029/2022GL099299, 2022.
 - Allen, R. G., Pereira, L. S., Raes, D., and Smith, M.: Crop evapotranspiration. Guidelines for computing crop water requirements, https://agris.fao.org/agris-search/search.do;jsessionid=5910CA98A93108675F0C1B03EFA8796F?request_locale=fr&recordID=XF1999085851&query=&sourceQuery=&sortField=&sortOrder=&agrovocString=&advQuery=¢erString=&enableField=, ISBN:
- 575 XF1999085851&query=&sourceQuery=&sortField=&sortOrder=&agrovocString=&advQuery=¢erString=&enableField=, ISBN: 9789251042199 Publisher: FAO, 1998.
 - Arce, M. I., Autrey, B., Baldwin, D. S., Bernal, S., Boersma, K. S., Bogan, M. T., Bonada, N., Bond, N., Bornette, G., Boulton, A. J., Carlson, S. M., Chauvet, E., Chester, E. T., Chiu, M.-C., Cid, N., Conallin, J., Corti, R., Costigan, K. H., Dahm, C. N., Datry, T., Wilde, M. D., Escoriza, D., Febria, C., Finn, D. S., Fritz, K., García-Berthou, E., Gido, K., Gómez, R., Heino, J., Hugueny, B., Jaeger, K. L.,
- Kennard, M. J., Kerezsy, A., Kingsford, R. T., Koundouri, P., Lake, P. S., Langhans, S. D., Leigh, C., Lytle, D. A., Magalhães, M. F., Martí, E., Mazor, R., McHugh, P. A., McIntosh, A. R., McLoughlin, C. A., Michaelides, K., Moleón, M., Monaghan, M. T., Mora-Gómez, J., Murphy, A. L., Norris, V., Reich, P., Resh, V., Risse-Buhl, U., Robson, B. J., Rolls, R. J., Romaní, A. M., Roux, D. J., Ruhi, A., Sabater, S., Sánchez-Montoya, M. M., Sánchez-Zapata, J. A., Sauquet, E., Singer, M., Skelton, P. H., Souliotis, I., Stella, J. C., Steward, A. L., Stromberg, J. C., Stubbington, R., Sutfin, N. A., Tedesco, P. A., Timoner, X., Tooth, S., Schiller, D. v., Vorste, R. V., Weitere, M., Whitney, J. E., and Zeglin, L.: Intermittent Rivers and Ephemeral Streams, in: Intermittent Rivers and Ephemeral Streams, edited by Datry, T.,
 - Aryal, S. K., Silberstein, R. P., Fu, G., Hodgson, G., Charles, S. P., and McFarlane, D.: Understanding spatio-temporal rainfall-runoff changes in a semi-arid region, 34, 2510–2530, https://doi.org/10.1002/hyp.13744, _eprint: https://onlinelibrary.wiley.com/doi/pdf/10.1002/hyp.13744, 2020.

Bonada, N., and Boulton, A., pp. xvii–xxi, Academic Press, https://doi.org/https://doi.org/10.1016/B978-0-12-803835-2.09996-4, 2017.

- Barnhart, K. R., Hutton, E. W. H., Tucker, G. E., Gasparini, N. M., Istanbulluoglu, E., Hobley, D. E. J., Lyons, N. J., Mouchene, M., Nudurupati, S. S., Adams, J. M., and Bandaragoda, C.: Short communication: Landlab v2.0: a software package for Earth surface dynamics, 8, 379–397, https://doi.org/https://doi.org/10.5194/esurf-8-379-2020, publisher: Copernicus GmbH, 2020.
 - Bierkens, M. F. P., Bell, V. A., Burek, P., Chaney, N., Condon, L. E., David, C. H., de Roo, A., Döll, P., Drost, N., Famiglietti, J. S., Flörke, M., Gochis, D. J., Houser, P., Hut, R., Keune, J., Kollet, S., Maxwell, R. M., Reager, J. T., Samaniego, L., Sudicky, E., Sutanudjaja, E. H., van de Giesen, N., Winsemius, H., and Wood, E. F.: Hyper-resolution global hydrological modelling: what is next?, 29, 310–320, https://doi.org/10.1002/hyp.10391, _eprint: https://onlinelibrary.wiley.com/doi/pdf/10.1002/hyp.10391, 2015.
 - Bonsor, H. C., MacDonald, A. M., Ahmed, K. M., Burgess, W. G., Basharat, M., Calow, R. C., Dixit, A., Foster, S. S. D., Gopal, K., Lapworth, D. J., Moench, M., Mukherjee, A., Rao, M. S., Shamsudduha, M., Smith, L., Taylor, R. G., Tucker, J., van Steenbergen, F., Yadav, S. K., and Zahid, A.: Hydrogeological typologies of the Indo-Gangetic basin alluvial aquifer, South Asia, 25, 1377–1406, https://doi.org/10.1007/s10040-017-1550-z, 2017.



605

610



- Brocca, L., Ciabatta, L., Massari, C., Camici, S., and Tarpanelli, A.: Soil Moisture for Hydrological Applications: Open Questions and New Opportunities, 9, 140, https://doi.org/10.3390/w9020140, number: 2 Publisher: Multidisciplinary Digital Publishing Institute, 2017.
- Carroll, R. W. H., Niswonger, R. G., Ulrich, C., Varadharajan, C., Siirila-Woodburn, E. R., and Williams, K. H.: Declining groundwater storage expected to amplify mountain streamflow reductions in a warmer world, 2, 419–433, https://doi.org/10.1038/s44221-024-00239-0, publisher: Nature Publishing Group, 2024.
- CGIAR-CSI: Global Aridity and PET Database, http://www.cgiar-csi.org/data/global-aridity-and-pet-database, 2009.
- Clark, M. P., Fan, Y., Lawrence, D. M., Adam, J. C., Bolster, D., Gochis, D. J., Hooper, R. P., Kumar, M., Leung, L. R., Mackay, D. S., Maxwell, R. M., Shen, C., Swenson, S. C., and Zeng, X.: Improving the representation of hydrologic processes in Earth System Models, 51, 5929–5956, https://doi.org/https://doi.org/10.1002/2015WR017096, _eprint: https://agupubs.onlinelibrary.wiley.com/doi/pdf/10.1002/2015WR017096, 2015.
- Cocking, K., Singer, M. B., MacLeod, D., Cuthbert, M. O., Rosolem, R., Muthusi, F., Paron, P., Kimutai, J., Omondi, P., Hassan, A. M., Teshome, A., and Michaelides, K.: Locally Defined Seasonal Rainfall Characteristics within the Horn of Africa Drylands from Rain Gauge Observations, https://doi.org/10.1175/JHM-D-23-0228.1, section: Journal of Hydrometeorology, 2024.
- Condon, L. E., Kollet, S., Bierkens, M. F. P., Fogg, G. E., Maxwell, R. M., Hill, M. C., Fransen, H.-J. H., Verhoef, A., Van Loon,
 A. F., Sulis, M., and Abesser, C.: Global Groundwater Modeling and Monitoring: Opportunities and Challenges, 57, e2020WR029500, https://doi.org/10.1029/2020WR029500, _eprint: https://onlinelibrary.wiley.com/doi/pdf/10.1029/2020WR029500, 2021.
 - Cuthbert, M. O., Gleeson, T., Moosdorf, N., Befus, K. M., Schneider, A., Hartmann, J., and Lehner, B.: Global patterns and dynamics of climate–groundwater interactions, 9, 137–141, https://doi.org/10.1038/s41558-018-0386-4, number: 2 Publisher: Nature Publishing Group, 2019.
- Dai, Y., Xin, Q., Wei, N., Zhang, Y., Shangguan, W., Yuan, H., Zhang, S., Liu, S., and Lu, X.: A Global High-Resolution Data Set of Soil Hydraulic and Thermal Properties for Land Surface Modeling, 11, 2996–3023, https://doi.org/https://doi.org/10.1029/2019MS001784, _eprint: https://agupubs.onlinelibrary.wiley.com/doi/pdf/10.1029/2019MS001784, 2019.
 - Dalcin, L. D., Paz, R. R., Kler, P. A., and Cosimo, A.: Parallel distributed computing using Python, Advances in Water Resources, 34, 1124–1139, https://doi.org/10.1016/j.advwatres.2011.04.013, 2011.
- Daron, J., Michaelides, K., Hassaballah, K., Quichimbo, A., Parfitt, R., Stacey, J., Steynor, A., Johnson, C., MacLeod, D., and Singer, M. B.: SIMBOL: A method to co-produce impact-based seasonal outlooks, 38, 100 579, https://doi.org/10.1016/j.cliser.2025.100579, 2025.
 - Dorigo, W., Wagner, W., Albergel, C., Albrecht, F., Balsamo, G., Brocca, L., Chung, D., Ertl, M., Forkel, M., Gruber, A., Haas, E., Hamer, P. D., Hirschi, M., Ikonen, J., de Jeu, R., Kidd, R., Lahoz, W., Liu, Y. Y., Miralles, D., Mistelbauer, T., Nicolai-Shaw, N., Parinussa, R., Pratola, C., Reimer, C., van der Schalie, R., Seneviratne, S. I., Smolander, T., and Lecomte, P.: ESA CCI Soil Moisture for improved Earth system understanding: State-of-the art and future directions, 203, 185–215, https://doi.org/10.1016/j.rse.2017.07.001, 2017.
 - Döll, P., Douville, H., Güntner, A., Schmied, H. M., and Wada, Y.: Modelling Freshwater Resources at the Global Scale: Challenges and Prospects, in: Remote Sensing and Water Resources, edited by Cazenave, A., Champollion, N., Benveniste, J., and Chen, J., no. 55 in Space Sciences Series of ISSI, pp. 5–31, Springer International Publishing, https://doi.org/10.1007/978-3-319-32449-4_2, 2016.
- Fan, Y., Li, H., and Miguez-Macho, G.: Global Patterns of Groundwater Table Depth, 339, 940–943, https://doi.org/10.1126/science.1229881, 2013.
 - Ferguson, G., Cuthbert, M. O., Befus, K., Gleeson, T., and McIntosh, J. C.: Rethinking groundwater age, 13, 592–594, https://doi.org/10.1038/s41561-020-0629-7, bandiera_abtest: a Cg_type: Nature Research Journals Number: 9 Primary_atype: Com-





- ments & Opinion Publisher: Nature Publishing Group Subject_term: Hydrology;Sustainability;Water resources Subject_term_id: hydrology;sustainability;water-resources, 2020.
- Gleeson, T., Moosdorf, N., Hartmann, J., and van Beek, L. P. H.: A glimpse beneath earth's surface: GLobal HYdrogeology MaPS (GLHYMPS) of permeability and porosity, 41, 3891–3898, https://doi.org/10.1002/2014GL059856, _eprint: https://onlinelibrary.wiley.com/doi/pdf/10.1002/2014GL059856, 2014.
 - Gleeson, T., Cuthbert, M., Ferguson, G., and Perrone, D.: Global Groundwater Sustainability, Resources, and Systems in the Anthropocene, 48, 431–463, https://doi.org/10.1146/annurev-earth-071719-055251, publisher: Annual Reviews, 2020.
- Godfrey, S., Hailemichael, G., and Serele, C.: Deep Groundwater as an Alternative Source of Water in the Ogaden Jesoma Sandstone Aquifers of Somali Region, Ethiopia, 11, 1735, https://doi.org/10.3390/w11081735, number: 8 Publisher: Multidisciplinary Digital Publishing Institute, 2019.
 - Goodrich, D. C., Lane, L. J., Shillito, R. M., Miller, S. N., Syed, K. H., and Woolhiser, D. A.: Linearity of basin response as a function of scale in a semiarid watershed, 33, 2951–2965, https://doi.org/10.1029/97WR01422, 1997.
- Gosling, S. N., Schmied, H. M., Betts, R., Chang, J., Chen, H., Ciais, P., Dankers, R., Döll, P., Eisner, S., Flörke, M., Gerten, D., Grillakis, M., Hagemann, S., Hanasaki, N., Huang, M., Huang, Z., Jerez, S., Kim, H., Koutroulis, A., Leng, G., Liu, J., Liu, X., Mao, G., Masaki, Y., Montavez, J. P., Morfopoulos, C., Oki, T., Orth, R., Ostberg, S., Papadimitriou, L., Pokhrel, Y., Portmann, F., Qi, W., Satoh, Y., Seneviratne, S., Sommer, P. S., Stacke, T., Tang, Q., Tsanis, I., Wada, Y., Wang, X., Zhou, T., Büchner, M., Schewe, J., and Zhao, F.: ISIMIP2a Simulation Data from the Global Water Sector, https://doi.org/10.48364/ISIMIP.882536, 2023a.
- Gosling, S. N., Schmied, H. M., Burek, P., Chang, J., Ciais, P., Döll, P., Eisner, S., Fink, G., Flörke, M., Franssen, W., Grillakis, M., Hagemann, S., Hanasaki, N., Koutroulis, A., Leng, G., Liu, X., Masaki, Y., Mathison, C., Mishra, V., Ostberg, S., Portmann, F., Qi, W., Sahu, R.-K., Satoh, Y., Schewe, J., Seneviratne, S., Shah, H. L., Stacke, T., Tao, F., Telteu, C., Thiery, W., Trautmann, T., Tsanis, I., Wanders, N., Zhai, R., Büchner, M., and Zhao, F.: ISIMIP2b Simulation Data from the Global Water Sector, https://doi.org/10.48364/ISIMIP.626689, 2023b.
- Guo, H., Hou, Y., Yang, Y., and McVicar, T. R.: Global Evaluation of Simulated High and Low Flows from 23 Macroscale Models, https://doi.org/10.1175/JHM-D-23-0176.1, section: Journal of Hydrometeorology, 2024.
 - Haas, H., Kalin, L., and Yen, H.: Improved forest canopy evaporation leads to better predictions of ecohydrological processes, Ecological Modelling, 489, 110 620, https://doi.org/10.1016/j.ecolmodel.2024.110620, 2024.
- Hobley, D. E. J., Adams, J. M., Siddhartha Nudurupati, S., Hutton, E. W. H., Gasparini, N. M., Istanbulluoglu, E., and Tucker, G. E.: Creative
 computing with Landlab: an open-source toolkit for building, coupling, and exploring two-dimensional numerical models of Earth-surface
 dynamics, 5, 21–46, https://doi.org/10.5194/esurf-5-21-2017, publisher: European Geosciences Union (EGU) / Copernicus Publications,
 2017.
 - Huffman, G. J., Bolvin, D. T., Braithwaite, D., Hsu, K., Joyce, R., Xie, P., and Yoo, S.-H.: NASA global precipitation measurement (GPM) integrated multi-satellite retrievals for GPM (IMERG), 4, 26, 2015.
- Idowu, T. E., Nyadawa, M., and K'Orowe, M. O.: Hydrogeochemical assessment of a coastal aquifer using statistical and geospatial techniques: case study of Mombasa North Coast, Kenya, 76, 422, https://doi.org/10.1007/s12665-017-6738-y, 2017.
 - Khazaei, B., Read, L. K., Casali, M., Sampson, K. M., and Yates, D. N.: GLOBathy, the global lakes bathymetry dataset, 9, 36, https://doi.org/10.1038/s41597-022-01132-9, number: 1 Publisher: Nature Publishing Group, 2022.





- Kozak, J. A., Ahuja, L. R., Green, T. R., and Ma, L.: Modelling crop canopy and residue rainfall interception effects on soil hydrological components for semi-arid agriculture, 21, 229–241, https://doi.org/10.1002/hyp.6235, _eprint: https://onlinelibrary.wiley.com/doi/pdf/10.1002/hyp.6235, 2007.
 - Leenaars, J. G. B., Claessens, L., Heuvelink, G. B. M., Hengl, T., Ruiperez González, M., van Bussel, L. G. J., Guilpart, N., Yang, H., and Cassman, K. G.: Mapping rootable depth and root zone plant-available water holding capacity of the soil of sub-Saharan Africa, 324, 18–36, https://doi.org/10.1016/j.geoderma.2018.02.046, 2018.
- Linke, S., Lehner, B., Ouellet Dallaire, C., Ariwi, J., Grill, G., Anand, M., Beames, P., Burchard-Levine, V., Maxwell, S., Moidu, H., Tan, F., and Thieme, M.: Global hydro-environmental sub-basin and river reach characteristics at high spatial resolution, 6, 283, https://doi.org/10.1038/s41597-019-0300-6, bandiera_abtest: a Cc_license_type: cc_publicdomain Cg_type: Nature Research Journals Number: 1 Primary_atype: Research Publisher: Nature Publishing Group Subject_term: Freshwater ecology; Hydrology Subject_term_id: freshwater-ecology; hydrology, 2019.
- Macdonald, A., Ó Dochartaigh, B., Bonsor, H., Davies, J., and Key, R.: Developing quantitative aquifer maps for Africa Groundwater Programme, https://doi.org/10.13140/RG.2.2.14589.26083, 2010.
 - MacDonald, A. M., Bonsor, H. C., Dochartaigh, B., and Taylor, R. G.: Quantitative maps of groundwater resources in Africa, 7, 024 009, https://doi.org/10.1088/1748-9326/7/2/024009, publisher: IOP Publishing, 2012.
- MacDonald, A. M., Lark, R. M., Taylor, R. G., Abiye, T., Fallas, H. C., Favreau, G., Goni, I. B., Kebede, S., Scanlon, B., Sorensen, J. P. R.,
 Tijani, M., Upton, K. A., and West, C.: Mapping groundwater recharge in Africa from ground observations and implications for water security, 16, 034 012, https://doi.org/10.1088/1748-9326/abd661, publisher: IOP Publishing, 2021.
 - MacLeod, D., Quichimbo, E. A., Michaelides, K., Asfaw, D. T., Rosolem, R., Cuthbert, M. O., Otenyo, E., Segele, Z., Rigby, J. M., Otieno, G., Hassaballah, K., Tadege, A., and Singer, M. B.: Translating seasonal climate forecasts into water balance forecasts for decision making, 2, e0000 138, https://doi.org/10.1371/journal.pclm.0000138, publisher: Public Library of Science, 2023.
- Mahoney, D. T., Christensen, J. R., Golden, H. E., Lane, C. R., Evenson, G. R., White, E., Fritz, K. M., D'Amico, E., Barton, C. D., Williamson, T. N., Sena, K. L., and Agouridis, C. T.: Dynamics of streamflow permanence in a headwater network: Insights from catchment-scale model simulations, 620, 129 422, https://doi.org/10.1016/j.jhydrol.2023.129422, 2023.
 - Martens, B., Miralles, D. G., Lievens, H., Schalie, R. v. d., Jeu, R. A. M. d., Fernández-Prieto, D., Beck, H. E., Dorigo, W. A., and Verhoest, N. E. C.: GLEAM v3: satellite-based land evaporation and root-zone soil moisture, 10, 1903–1925, https://doi.org/10.5194/gmd-10-1903-2017, publisher: Copernicus GmbH, 2017.
 - Marçais, J., de Dreuzy, J. R., and Erhel, J.: Dynamic coupling of subsurface and seepage flows solved within a regularized partition formulation, 109, 94–105, https://doi.org/10.1016/j.advwatres.2017.09.008, 2017.
 - Menzel, L.: Modellierung der evapotranspiration im system boden-pflanze-atmosphäre, PhD Thesis, ETH Zurich, 1996.
- Messager, M. L., Lehner, B., Cockburn, C., Lamouroux, N., Pella, H., Snelder, T., Tockner, K., Trautmann, T., Watt, C., and Datry, T.:

 Global prevalence of non-perennial rivers and streams, 594, 391–397, https://doi.org/10.1038/s41586-021-03565-5, bandiera_abtest: a

 Cg_type: Nature Research Journals Number: 7863 Primary_atype: Research Publisher: Nature Publishing Group Subject_term: Geography;Hydrology;Limnology;Water resources, 2021.
- Moeck, C., Grech-Cumbo, N., Podgorski, J., Bretzler, A., Gurdak, J. J., Berg, M., and Schirmer, M.: A global-scale dataset of direct natural groundwater recharge rates: A review of variables, processes and relationships, 717, 137 042, https://doi.org/10.1016/j.scitotenv.2020.137042, 2020.





- Niazi, H., Wild, T. B., Turner, S. W. D., Graham, N. T., Hejazi, M., Msangi, S., Kim, S., Lamontagne, J. R., and Zhao, M.: Global peak water limit of future groundwater withdrawals, 7, 413–422, https://doi.org/10.1038/s41893-024-01306-w, publisher: Nature Publishing Group, 2024.
- Palmer, P. I., Wainwright, C. M., Dong, B., Maidment, R. I., Wheeler, K. G., Gedney, N., Hickman, J. E., Madani, N., Folwell, S. S., Abdo,
 G., Allan, R. P., Black, E. C. L., Feng, L., Gudoshava, M., Haines, K., Huntingford, C., Kilavi, M., Lunt, M. F., Shaaban, A., and Turner,
 A. G.: Drivers and impacts of Eastern African rainfall variability, 4, 254–270, https://doi.org/10.1038/s43017-023-00397-x, publisher:
 Nature Publishing Group, 2023.
 - Peel, M. C., Finlayson, B. L., and McMahon, T. A.: Updated world map of the Köppen-Geiger climate classification, 11, 1633–1644, https://doi.org/10.5194/hess-11-1633-2007, publisher: Copernicus GmbH, 2007.
- Quichimbo, E. A., Singer, M. B., and Cuthbert, M. O.: Characterising groundwater–surface water interactions in idealised ephemeral stream systems, 34, 3792–3806, https://doi.org/10.1002/hyp.13847, eprint: https://onlinelibrary.wiley.com/doi/pdf/10.1002/hyp.13847, 2020.
 - Quichimbo, E. A., Cuthbert, M. O., Singer, M. B., Michaelides, K., Rosolem, R., and Hobley, D. E. J.: DRYP 1.0: A parsimonious hydrological model of DRYland Partitioning of the water balance, https://doi.org/10.5281/ZENODO.5061987, language: en, 2021.
- Quichimbo, E. A., Singer, M. B., Michaelides, K., Rosolem, R., MacLeod, D. A., Asfaw, D., and Cuthbert, M. O.: Assessing the sensitivity of modelled water partitioning to global precipitation datasets in a data-scarce dryland region, 37, e15 047, https://doi.org/10.1002/hyp.15047, _eprint: https://onlinelibrary.wiley.com/doi/pdf/10.1002/hyp.15047, 2023.
 - Quichimbo, E. A., Singer, M., Michaelides, K., and Cuthbert, M.: DRYP 2.0: A hydrological model for local and regional scale across aridity gradients, https://doi.org/10.5281/zenodo.17451148, 2025.
- Quiroga, E., Bertoni, C., van Goethem, M., Blazevic, L. A., and Ruden, F.: A 3D geological model of the horn of Africa: New insights for hydrogeological simulations of deep groundwater systems, 42, 101 166, https://doi.org/10.1016/j.ejrh.2022.101166, 2022.
 - Save, H., Bettadpur, S., and Tapley, B. D.: High-resolution CSR GRACE RL05 mascons, 121, 7547–7569, https://doi.org/10.1002/2016JB013007, _eprint: https://agupubs.onlinelibrary.wiley.com/doi/pdf/10.1002/2016JB013007, 2016.
 - Schreiner-McGraw, A., Ajami, H., and Vivoni, E. R.: Extreme weather events and transmission losses in arid streams, 14, 084 002, https://doi.org/10.1088/1748-9326/ab2949, 2019.
- Shanafield, M., Niswonger, R. G., Prudic, D. E., Pohll, G., Susfalk, R., and Panday, S.: A method for estimating spatially variable seepage and hydraulic conductivity in channels with very mild slopes, 28, 51–61, https://doi.org/10.1002/hyp.9545, 2014.
 - Shanafield, M., Bourke, S. A., Zimmer, M. A., and Costigan, K. H.: An overview of the hydrology of non-perennial rivers and streams, 8, e1504, https://doi.org/10.1002/wat2.1504, _eprint: https://onlinelibrary.wiley.com/doi/pdf/10.1002/wat2.1504, 2021.
- Singer, M. B., Asfaw, D. T., Rosolem, R., Cuthbert, M. O., Miralles, D. G., MacLeod, D., Quichimbo, E. A., and Michaelides, K.: Hourly
 potential evapotranspiration at 0.1° resolution for the global land surface from 1981-present, 8, 224, https://doi.org/10.1038/s41597-02101003-9, bandiera_abtest: a Cc_license_type: cc_publicdomain Cg_type: Nature Research Journals Number: 1 Primary_atype: Research
 Publisher: Nature Publishing Group Subject_term: Hydrology Subject_term_id: hydrology, 2021.
 - Taylor, R. G., Todd, M. C., Kongola, L., Maurice, L., Nahozya, E., Sanga, H., and MacDonald, A. M.: Evidence of the dependence of groundwater resources on extreme rainfall in East Africa, 3, 374–378, https://doi.org/10.1038/nclimate1731, number: 4 Publisher: Nature Publishing Group, 2013.
 - Telteu, C.-E., Müller Schmied, H., Thiery, W., Leng, G., Burek, P., Liu, X., Boulange, J. E. S., Seaby Andersen, L., Grillakis, M., Gosling, S. N., Satoh, Y., Rakovec, O., Stacke, T., Chang, J., Wanders, N., Shah, H. L., Trautmann, T., Mao, G., Hanasaki, N., Koutroulis, A., Pokhrel, Y., Samaniego, L., Wada, Y., Mishra, V., Liu, J., Döll, P., Zhao, F., Gädeke, A., Rabin, S., and Herz, F.: Understanding each



755

760



- other's models: a standard representation of global water models to support improvement, intercomparison, and communication, pp. 1–56, https://doi.org/10.5194/gmd-2020-367, publisher: Copernicus GmbH, 2021.
 - Vegas Galdos, F., Álvarez, C., García, A., and Revilla, J. A.: Estimated distributed rainfall interception using a simple conceptual model and Moderate Resolution Imaging Spectroradiometer (MODIS), 468-469, 213–228, https://doi.org/10.1016/j.jhydrol.2012.08.043, 2012.
 - Verkaik, J., Sutanudjaja, E. H., Oude Essink, G. H. P., Lin, H. X., and Bierkens, M. F. P.: GLOBGM v1.0: a parallel implementation of a 30 arcsec PCR-GLOBWB-MODFLOW global-scale groundwater model, 17, 275–300, https://doi.org/10.5194/gmd-17-275-2024, publisher: Copernicus GmbH, 2024.
 - von Hoyningen-Huene, J.: Die Interzeption des Niederschlags in landwirtschaftlichen Pflanzenbeständen, Arbeitsbericht Deutscher Verband für Wasserwirtschaft und Kulturbau, DVWK, 1981.
 - Wainwright, C. M., Marsham, J. H., Keane, R. J., Rowell, D. P., Finney, D. L., Black, E., and Allan, R. P.: 'Eastern African Paradox' rainfall decline due to shorter not less intense Long Rains, 2, 1–9, https://doi.org/10.1038/s41612-019-0091-7, publisher: Nature Publishing Group, 2019.
 - Xie, J., Liu, X., Jasechko, S., Berghuijs, W. R., Wang, K., Liu, C., Reichstein, M., Jung, M., and Koirala, S.: Majority of global river flow sustained by groundwater, pp. 1–8, https://doi.org/10.1038/s41561-024-01483-5, publisher: Nature Publishing Group, 2024.
 - Zaherpour, J., Gosling, S. N., Mount, N., Schmied, H. M., Veldkamp, T. I. E., Dankers, R., Eisner, S., Gerten, D., Gudmundsson, L., Haddeland, I., Hanasaki, N., Kim, H., Leng, G., Liu, J., Masaki, Y., Oki, T., Pokhrel, Y., Satoh, Y., Schewe, J., and Wada, Y.: Worldwide evaluation of mean and extreme runoff from six global-scale hydrological models that account for human impacts, 13, 065 015, https://doi.org/10.1088/1748-9326/aac547, publisher: IOP Publishing, 2018.
 - Zarate, E., Cuthbert, M. O., Chappell, A., MacDonald, A. M., and Quichimbo, E. A.: The role of superficial geology in controlling riparian water availability beneath dryland ephemeral streams, pp. 311–04, 2022.
- Zoccatelli, D., Marra, F., Armon, M., Rinat, Y., Smith, J. A., and Morin, E.: Contrasting rainfall-runoff characteristics of floods in desert and Mediterranean basins, 23, 2665–2678, https://doi.org/https://doi.org/10.5194/hess-23-2665-2019, publisher: Copernicus GmbH, 2019.